12-14-2015

Molecules and Metals in the Distant Universe: Sub-MM and Optical Spectroscopy of Quasar Absorbers

Sean Stephen Morrison
University of South Carolina - Columbia

Recommended Citation

Morrison, S. S.(2015). *Molecules and Metals in the Distant Universe: Sub-MM and Optical Spectroscopy of Quasar Absorbers.* (Master's thesis). Retrieved from https://scholarcommons.sc.edu/etd/3200

Molecules and Metals in the Distant Universe: Sub-mm and Optical Spectroscopy of Quasar Absorbers

by

Sean Stephen Morrison

Bachelor of Science
Appalachian State University 2011

Submitted in Partial Fulfillment of the Requirements

for the Degree of Master of Science in

Physics

College of Arts and Sciences

University of South Carolina

2015

Accepted by:

Varsha Kulkarni, Director of Thesis

Richard Creswick, Reader

Lacy Ford, Senior Vice Provost and Dean of Graduate Studies

ACKNOWLEDGMENTS

I would like to thank all those without whose help and support this work would not be possible. First off, I wish to thank my advisor, Dr. Varsha P. Kulkarni, for her tutelage, patience, encouragement and constant support. I would also like to thank my committee member Dr. Richard Creswick for his time, interest and valuable suggestions. I am greatly indebted to my collaborators, Dr. Debopam Som, Dr. Monique Aller, and Dr. Celine Péroux who helped me immeasurably with this work. I would like to thank my family, friends, and especially my wife, Mandy, for the support and understanding they have all shown.

I would like to thank all the present and former graduate students in our Astronomy group, especially, Francie Cashman, Suraj Poudel, Nassim Beiranvand, and Dr. Lorrie Straka, for their friendship, collaboration and encouragement.

I would like to express my gratitude towards National Science Foundation, National Aeronautics and Space Administration, Space Telescope Science Institute, and National Optical Astronomy Observatory for providing support to this work. Finally, I sincerely thank the staff at the Keck Observatory and Herschel Space Observatory for their help in carrying out the observations that this work is largely based upon.

ABSTRACT

In order to gain a complete understanding of galaxy formation and evolution, knowledge of the atomic and molecular gas in the interstellar medium (ISM) is required. Absorption-line spectroscopy of quasars offers a powerful and luminosity independent probe of gas in distant galaxies. The Damped Lyman-α systems (DLAs; $20.3 \lesssim \log N_{HI}$), are the highest neutral hydrogen column density quasar absorbers and contain a substantial fraction of the neutral gas available for star formation in the high-redshift Universe.

This thesis presents a study of the metal content in some DLAs, based on optical spectroscopy, and a search for molecules based on sub-mm observations. For the sub-mm sample, spectra for 5 quasars with absorbers ($0.524 < z_{abs} < 1.173$) were taken with SPIRE and Heterodyne Instrument for the far-infrared (HIFI) on Herschel. These observations, in the far-IR and sub-mm bands, were optimized for detection of molecular lines of CO, ^{13}CO, C^{18}O, H_2O, HCO, and the forbidden transitions of [C II] and [N II]. Two targets, the DLA towards PKS0420-014 at $z = 0.633$ and the DLA towards AO0235+164 at $z = 0.524$, showed very tentative detections of C^{18}O, and another, the DLA towards TXS0827+243 at $z = 0.52476$, showed a very tentative detection HCO. We report 3 σ upper limits for several other molecules.

Two especially gas-rich DLAs ("super-DLAs") with $z = 2.5036$ and $z = 2.045$ were observed using the echellette mode on Keck Echellette Spectrograph and Imager (ESI). These observations were optimized to detect a number of metal lines. Both absorbers show remarkably similar metallicities of ~ -1.3 to ~ -1.4 dex and comparable, definitive depletion levels, as judged from [Fe/Zn] and [Ni/Zn]. One of the absorbers shows supersolar [S/Zn] and [Si/Zn]. Using potential detections of weak Ly-α emission at the bottom of the DLA trough for Q0230-0334, we estimate star formation rates in the absorbers to be $\sim$1.6 M$_\odot$ yr^{-1}. Finally, measurements of the absorption line velocity spread, Δv_{90}, suggest that super-DLAs may have narrower velocity dispersions and may arise in cooler and/or less turbulent gas.

TABLE OF CONTENTS

List of Tables

LIST OF FIGURES

CHAPTER 1

INTRODUCTION

An understanding of our universe and how it has evolved is one of humankind's pressing questions. Over the last several decades significant advances have been made towards an understanding of the galaxy formation and evolution though the use of observations and models. However, we have yet to obtain a clear picture of the earliest epochs of the universe. To gain this understanding, observations of molecules and atoms, especially metals (elements with atomic weight greater than that of Helium), in the distant universe are necessary. As stars, and galaxies, have formed and evolved, the chemical makeup of the universe has evolved due to stellar nucleosynthesis (s- and r-process and fusion), supernova explosions, stellar winds, and molecular condensation.

1.1 METALS IN THE DISTANT UNIVERSE

The big bang nucleosynthesis produced baryonic matter in the form of Hydrogen, Helium, and trace amounts of Lithium due to the temperatures for the creation of stable nuclei of the various elements. As the Universe evolved and formed stars and galaxies, "metals" (elements heavier than H and He in the language of Astronomy) were formed in stars. The production of different metals is dependent on stellar masses and the life cycles of the stars.

Due to the dependence on stellar mass and stellar life cycles, different elements are released into the ISM on different timescales based on the production, ejection and mixing mechanisms. In addition, the next generation of stars is formed from

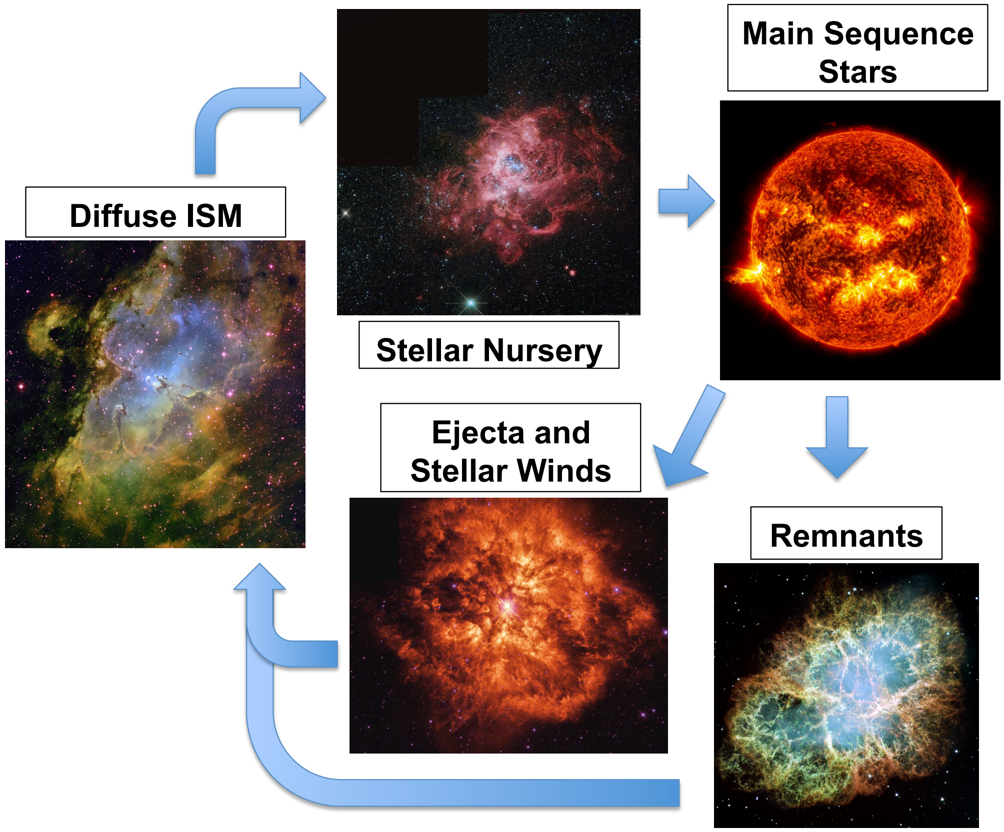

Figure 1.1 A schematic representation of how star formation cycles in galaxies connect stars with the chemical enrichment of the interstellar medium.

this enriched ISM, which continues the cycle as shown in Fig. 1.1. Stellar winds and supernova explosions are the main sources for the heavy metal enrichment of the ISM.

Stellar winds, especially in the form of 'planetary nebulae', mainly release light elements such as He, C, N, and O (van den Hoek and Groenewegen, 1997) into the ISM. Supernova are the primary source of heavier metals. Type II supernova nucleosynthesis results in the overproduction of C and α-capture elements (O, Mg, SI, S, Ca, Ar, etc.) relative to Fe. While Type Ia supernova nucleosynthesis produces the Fe-peak elements (Cr, Mn, Fe, Co, and Zn).

These metals in the ISM are detected as absorption lines in the continuum of background sources (such as Quasars and GRBs).

1.2 Molecules in the Distant Universe

Interstellar molecules are essential to a complete understanding of astrophysics. They are found in a variety of environments and can be used to probe the physical condition in those environments. The large number of molecular absorption lines in the interstellar medium (ISM) provide detailed information about the physical and chemical properties of the cold, dense regions. An understanding of the properties and the molecular content in distant galaxies is essential to a complete understanding of the cosmic star formation history. Molecular clouds, the progenitors of stars, are a mix of atomic He and molecular gas (Omont, 2007) at a density of $\sim 10^3$ cm^{-3}. This molecular gas is composed of $\sim 100\%$ H_2 with $< 1\%$ being CO and H_2O (Omont, 2007). These clouds collapse into dense accretion discs with a molecular flows pre-planetary discs. Since molecules are a small portion of the ISM, they have very little influence on the physical properties of the ISM and its evolution. However, they can act as probes of the ISM, especially in the infrared range of the spectra.

The molecular gas traces the densest regions of gas, therefore it is important to study them as they hold significant concentrations of gas. The properties, including distribution and quantities, of the molecular gas is essential for understanding star formation and galaxy evolution.

In the local ISM ~ 150 species of molecules have been identified (Omont, 2007). These have been formed mainly of H, C, O, and N atoms with some occurrences of S, Si, and other metals. These molecules come in two varieties, large (~ 10 atoms) and exotic unstable species. These exotic compounds are directly linked to low interstellar densities. In regions of the ISM with 'normal' elemental abundances ($C/O < 1$), the dominant molecules, after H_2, are CO and H_2O (Omont, 2007).

The earliest CO surveys shows a strong correlation between the CO intensities and both far-infrared and Hα luminosities

The correlation between CO intensities and far-infrared luminosities, as well as Hα luminosities, has been seen since the earliest extragalactic CO surveys (Omont, 2007). CO lines, due to their lack of extinction, probe massive starbursts at high redshifts. The profiles of the CO lines can provide molecular and dynamical masses of starburst galaxies. This offers an insight into past and future star formation.

Due to difficulties in detecting H_2 in the normal ISM, most of the knowledge of molecular gas comes from CO observations (Omont, 2007). However, these observations rely on background sources, such as hot stars or quasars, to illuminate the gas. The independence of absorption line strengths with distance makes the use of absorption lines, especially at high redshift, the ideal tool with which to study molecular gas. While detecting emission at high-z is difficult, especially in front of bright background sources, such as Quasars, absorption lines provide a powerful tool to analyze the ISM.

Quasar Absorption systems, in particular damped Lyman-α (DLA) absorber (log $N_{HI} \geq 20.3$), are excellent direct probes of the ISM in high-z galaxies. DLAs are the primary neutral gas reservoir available for star formation and the complement emission-line abundances to offer the most precise elemental abundance measurements in distant galaxies.

The strong infrared continuum sources of active galactic nuclei (AGN) seem to be ideal for tracing absorption of molecules in obscured sources. However infrared spectroscopic surveys of AGN have found few absorption features in a few sources (Omont, 2007).

1.3 Quasar Absorption Systems

When Quasars were first discovered, they were named Quasi-Stellar Objects (QSOs) due to their star like appearance in images, however, they showed very different spectral colors from stars. Farther exploration of the objects found them to be extra-

Galactic in origin, which implied they couldn't be stars due to the required intrinsic (distance-corrected) luminosities. Therefore they were called quasi-stellar objects, or QSOs. Their typical luminosities are greater than the entire Milky Way ($\sim 10^{46}$ ergs s^{-1}) with an emitting region of sub-parsec scale (based on the time scales of flux variations, typically on the order of weeks). This energy output from such a small region, and the presence of broad emission lines in the spectra indicates relativistic processes at work, with the presently accepted model being an accreting super-massive black hole ($M_{BH} \sim 10^6 - 10^9 M_\odot$). Quasars, or "quasi-stellar radio sources" are a subset of QSOs that are also radio sources. The continuum of a typical quasar can be fit by power law functions of the form $F_\nu \propto \nu^\alpha$ with an index $\alpha \sim -1$ (Zheng et al., 1997).

Quasars are the farthest know sources with the most distant being $z = 7.1$ (Momjian et al., 2014), with more then 200,000 quasars identified (York et al., 2000). Therefore, they have been used as background sources for absorption line studies of the Universe at the largest scale.

1.3.1 LYMAN-α ABSORPTION IN QUASAR SPECTRA

When a quasar sight line interacts with an intervening gas cloud such as the intergalactic medium, circumgalactic medium, and the ISM in galaxies it will leave a distinct absorption profile on the continuum that is dependent on densities and temperatures. This process is illustrated in the schematic representation of the line of sight towards a quasar with the corresponding observed spectrum shown in Fig. 1.2. The board emission peak at $\sim$ 4900 Å represents the Hydrogen emission from the quasar and the strong Hydrogen absorption line at $\sim$ 4700 Å is produced by an intervening galaxy. Also shown are narrow metal absorption lines from the intervening galaxy to the right of the emission peak and numerous other Hydrogen absorption features of various strengths to the left of the peak. Hydrogen lines, with Hydrogen being the most abundant element in the Universe, are the most common among the

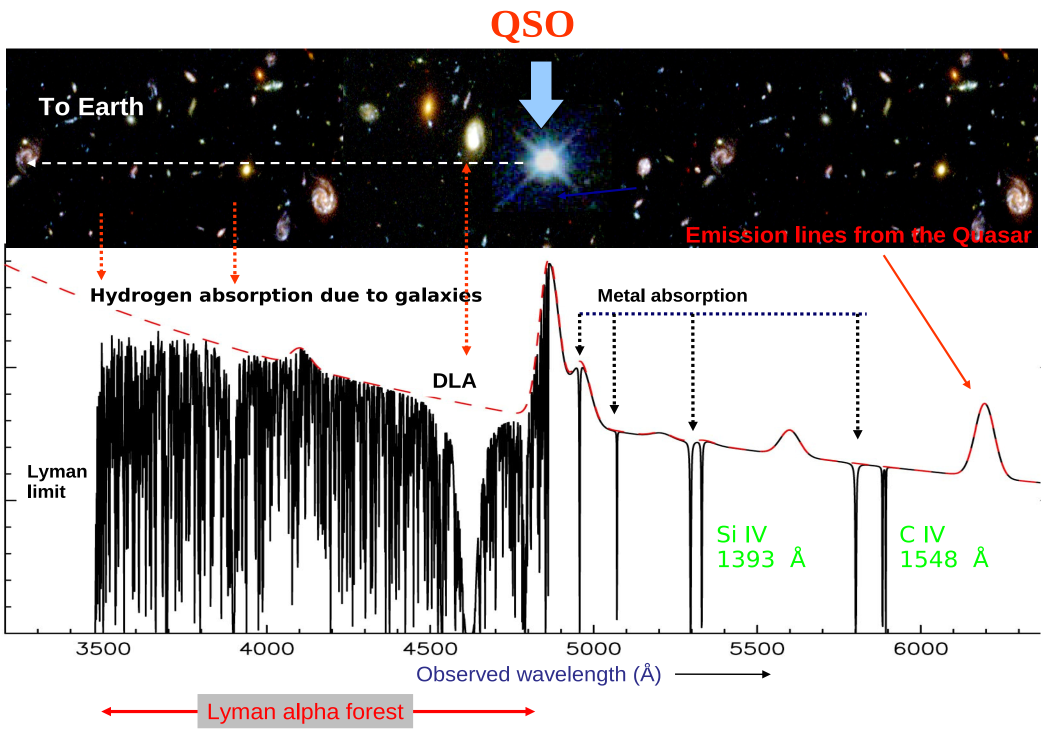

Figure 1.2 A schematic representation of the quasar absorption line technique illustrating the absorption, and corresponding lines, by galaxies and gas along the quasar sightline and spectra. This representation is created from a version produced by John Webb and published in Pettini (2004).

different absorption features seen in quasar spectra. Most of the Hydrogen lines seen, as most of the neutral Hydrogen atoms are in the ground state, are from the Lyman-series transitions. The most common of these transitions seen in quasar spectra is the Lyman-α transition ($n = 1 \rightarrow 2$) at 1215.6701 Å (the strongest of the series).

Different absorption systems can be broadly classified into four categories (see Table 1.1) based on their neutral Hydrogen column densities derived from the Lyman-α lines. Systems with log N_{HI} >19.0 trace large amounts of neutral gas and are believed to be associated with galaxies along the line of sight and thus are extremely important systems to study for chemical evolution studies. They are believed to contain the majority of the neutral gas in the Universe. These systems are sub-

Table 1.1 The classification, based on N_{HI}, of absorption systems seen in quasar spectra.

Column Density	Classification
log N_{HI} <17.2	Lyman-α forest
17.2 $\lesssim$ log N_{HI} $\lesssim$ 19.0	Lyman Limit System (LLS)
19.0 $\lesssim$ log N_{HI} $\lesssim$ 20.3	sub-Damped Lyman-α (sub-DLA)
20.3 $\lesssim$ log N_{HI}	Damped Lyman-α (DLA)

divided into two classes: the sub-damped Lyman-α systems ($19.0 \leq \log N_{HI} < 20.3$) or sub-DLAs, and the damped Lyman-α systems ($20.3 \lesssim \log N_{HI}$) or DLAs. The boundary ($N_{HI} = 10^{20.3}$) between sub-DLAs and DLAs is arbitrary and historically resulted from the initial DLA surveys carried out with low-resolution spectrographs, where this column density represents the lower limit of the strengths of the features detected in these studies. In addition, we defined the strongest DLAs, with the arbitrary boundary $N_{HI} = 10^{21.7}$, as super-DLAs.

In addition to the Lyman-α line, absorption features corresponding to various elements are seen in quasar absorption systems. These can include elements such as Ar, C, N, O, P, Mg S, Si, Ca, Ti, Cr, Mn, Ni, Fe, and Zn. Lines of these elements can be fit with Voigt profiles (Appendix D) to determine chemical abundances in the systems using Eqs. C.18 and C.19.

Lyman-α forest systems

Lyman-α forest systems are weak Lyman-α absorption systems (log N_{HI} <17.2) whose features are ubiquitously seen blueward of the Lyman-α emission peak in the quasar spectra. They are thought to be identified with intergalactic gas clouds due to the number of the absorbers and their weak clustering properties (Rouch, 1998).

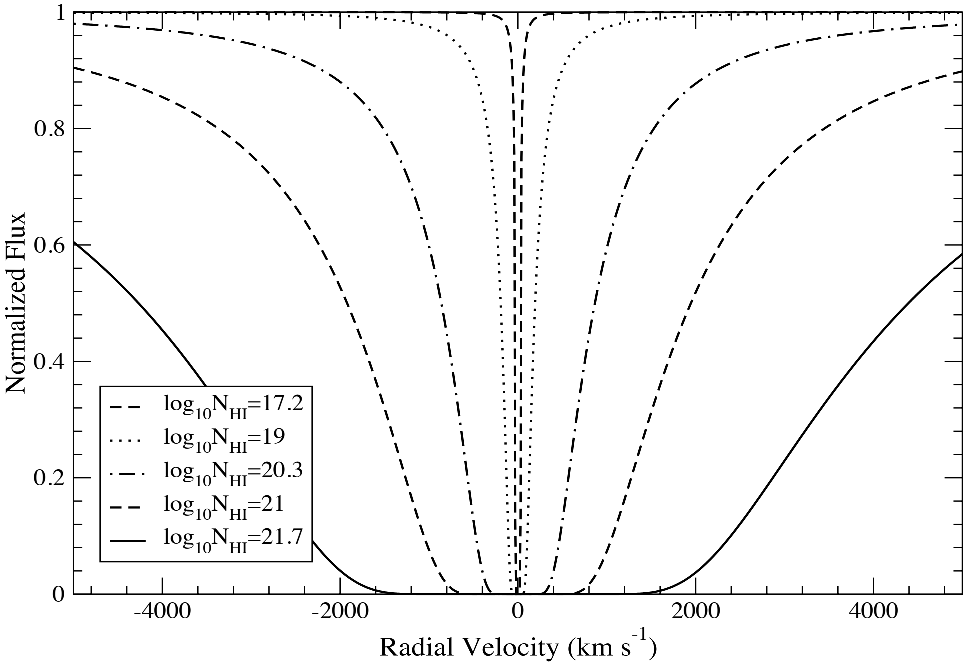

Figure 1.3 Theoretical Voigt profiles for the H I Lyman-α transition for column densities of $10^{17.2}$, 10^{19}, $10^{20.3}$, 10^{21} and $10^{21.7}$ cm^{-2} with a fixed $b = 10kms^{-1}$. The Lorentzian profile increasingly dominates the Voigt profile with rising N_{HI} causing the damping wings that starts to become evident for log $N_{HI} \gtrsim 19.0$

LYMAN LIMIT SYSTEM (LLS)

Lyman Limit Systems (LLS) ($17.2 \lesssim \log N_{HI} \lesssim 19.0$) contain denser and more neutral gas compared to Lyman-α forest systems. Hydrogen clouds become optically thick ($\tau = 1.0$) at the limit of the Hydrogen Lyman series (912 Å). They are believed to trace the circumgalactic medium (Lehner et al., 2013; Steidel, 1990).

SUB-DAMPED LYMAN-α ABSORBERS (SUB-DLAS)

Sub-Damped Lyman-α Absorbers (sub-DLAs) with $19.0 \lesssim \log N_{HI} \lesssim 20.3$, are thought to be the progenitors of massive galaxies which convert their gas mass into stars at an earlier epoch than the DLA galaxies (Kulkarni et al., 2010).

DAMPED LYMAN-α ABSORBERS (DLAS)

Damped Lyman-α Absorbers (DLAs) with $20.3 \lesssim \log N_{HI}$, are thought to be the progenitors to galaxies, smaller then Sub-DLAs, which are still in the process of converting their gas mass into stars (Kulkarni et al., 2010), and are suspected to be analogous to the disks of nearby luminous galaxies at high-redshift (Khare et al., 2007). They, along with Sub-DLAs, are thought to be the primary reservoirs of neutral gas in the early universe (Storrie-Lombardi and Wolfe, 2000; Péroux et al., 2003).

Super-Damped Lyman-α Absorbers (Super-DLAs)

Super-Damped Lyman-α Absorbers (Super-DLAs), with $\log N_{HI} > 21.7$, are a subset of DLAs with very high H I column densities and are thought to be progenitors of galaxies with large N_{HI} reservoirs. Fewer super-DLAs have been detected than DLAs and sub-DLAs. Despite their small numbers, these extremely gas-rich systems may contribute 10% of the comoving neutral gas density (Noterdaeme et al., 2012a; Noterdaeme et al., 2014). One theory is that the large H I column densities could be the result of large structures, ie. large masses of absorbing galaxies. Measurements of absorption line profiles, which can yield velocity dispersion data, can clarify the situation as large scale structures should exhibit large velocity dispersion.

Kulkarni et al. (2012) and Noterdaeme et al. (2012b) carried out the first detailed studies of an intervening quasar super-DLA, a $z = 2.2$ absorber toward SDSSJ1135-0010, using the Very Large Telescope (VLT) Ultraviolet-Visual Echelle Spectrograph (UVES) and X-shooter. This super-DLA is fairly enriched, with $[\mathrm{Zn/H}] = -1.06 \pm 0.10$, $[\mathrm{Si/H}] = -1.10 \pm 0.10$, $[\mathrm{Cr/H}] = -1.55 \pm 0.10$, $[\mathrm{Ni/H}] = -1.60 \pm 0.10$, $[\mathrm{Fe/H}] = -1.76 \pm 0.10$, $[\mathrm{Ti/H}] = -1.69 \pm 0.11$, $[\mathrm{P/H}] = -0.93 \pm 0.23$, and $[\mathrm{Cu/H}] = -0.75 \pm 0.14$. Furthermore, it shows strong Ly-α emission near the bottom of the DLA trough and other nebular emission lines, implying a fairly high SFR of $\sim 25\ \mathrm{M}_{\odot}\ \mathrm{yr}^{-1}$. The Ly-$\alpha$

emission shows two distinct peaks (each $> 7\sigma$), possibly suggesting outflowing gas (Noterdaeme et al., 2012b).

Noterdaeme et al. (2014) showed that, when stacked, SDSS spectra of Super-DLA absorbers, when shifted to the absorber rest-frame, shows a statistical detection Lyman-α emission at the bottom of the DLA trough. This suggests a strong association with Lyman-α emission with a small impact parameter so that the emission falls in the SDSS fiber. In addition, some of the super-DLAs have shown indications of being rich in molecular gas (e.g., Guimaraes et al., 2012; Noterdaeme, Petitjean, and Srianand, 2015b).

CHAPTER 2

MOLECULAR ABSORPTION IN DLAS AND OTHER QUASAR ABSORBERS

Our sample consisted of 5 absorbers at $z_{abs} < 1.5$ with bright background quasars. These absorbers have previously shown evidence of metal-rich, cold ISM. This evidence is from strong metal lines, low spin temperatures from the 21-cm absorption line, and/or detections of molecules in mm and radio observations (Wiklind and Combes, 1996; Wiklind and Combes, 1998; Menten et al., 2008). The quasars show highly reddened spectra and some dust features from carbonaceous and/or silicate dust at the absorbers redshift (Junkkarinen et al. 2004; Kulkarni et al. 2007, 2011; Aller et al. 2011). PKS1830-211 is a gravitationally lensed quasar, though at Herschel's resolution the two lensed images are not separable. Differential photometry on PKS1830-211 has yielded the dust extinction curve of the foreground absorbing galaxy. In some of the absorbers, molecular transitions have been previously detected in radio. These detections suggest molecular fractions of $\sim 0.3 - 1.0$. This fraction is thousands of times higher then the typical DLA.

Hershel HIFI (Heterodyne Instrument for the Far Infrared) is a high resolution spectrograph that covers $490 - 1250$ GHz and $1410 - 1910$ GHz. It consists of 4 spectrometers: 2 HRS (High Resolution Spectrometers) with a resolution of 0.25MHz, and 2 WBS (Wide-Band Spectrometers) with a resolution of 1.1MHz. Our observations were obtained using the single point mode. Herschel SPIRE (Spectral and Photometric Imaging Receiver) consists of two separate modes, a spectral imaging mode

Table 2.1 Spectroscopic Targets for Herschel Observations With HIFI and SPIRE

Quasar	z_{em}	z_{abs}	log N_{21}	τ_{21}	Known Features
AO0235+164	0.940	0.52385	21.70	0.64	X-ray abs., DIBS
PKS0420-014	0.916	0.633			Strong Mg II abs., Mg I, Fe III
TXS0827+243	0.940	0.52476	20.30	0.007	Strong Mg II II, Fe II abs.
PKS1830-211	2.507	0.88583	21.24	0.055	9.7μm abs., molecules
PKS2355-106	1.638	1.17260	$\geq$20.07	0.035	Strong Mg II II, Fe II, Zn II abs.

and a photometric imaging mode. We utilized the photometric imaging mode for flux calibration of our spectroscopic targets and to identify bright targets for future observations. The spectral imaging mode is a low resolution point source spectrograph ($\Delta v = 300$ km/s) that covers $194 - 313$ μm and $303 - 671$ μm.

From the Herschel OT1 proposal, OT1_vkulkarn_1, we obtained 10 Hifi Point spectroscopic observations of molecules in distant damped Lyα quasar absorbers (Tables 2.1). These high-resolution HIFI observations cover specific absorption lines of CO, CN, NH, and H_2O.

The 10 Hifi point spectra were of 4 quasars: AO0235+164 ($z_{abs} = 0.52385$), TXS0827+243 ($z_{abs} = 0.52476$), PKS 1830-211 ($z_{abs} = 0.88583$), and PKS2355-106 ($z_{abs} = 1.17260$) (Table 2.1). These observations targeted the transitions of several atomic and molecular not accessible from the ground in the gap between the optical/near-IR/mid-IR range and the radio range. These lines include lines of [C II], [N II], CO, ^{13}CO, C^{18}O, H_2O.

From the follow up Herschel OT2 proposal, OT2_vkulkarn_3, we obtained 5 Spire spectroscopic point observations. These Spire spectroscopy observations were of 5 quasars with z_{abs} ranging from 0.52385 to 1.17260: PKS1830-211 ($z_{abs} = 0.88583$), TXS0827+243 ($z_{abs} = 0.52476$), PKS2355-106 ($z_{abs} = 1.17260$), AO0235+164 ($z_{abs} = 0.52385$), and PKS0420-014 ($z_{abs} = 0.633$).

2.1 Data Reduction and Analysis

The data reduction and analysis is a multi-step process involving the Herschel Interactive Processing Environment, IRAF, and post IRAF reduction and analysis tools.

2.1.1 Herschel Interactive Processing Environment

Using the Herschel Interactive Processing Environment, HIPE, data processing pipeline we have confirmed the automated HIPE reductions of the 5 objects. For the HIFI observations we ran two additional post processing steps in HIPE: fitHifiFringe and fitBaseline. The fitHifiFringe tool was used to fit and subtract a set of sine waves to the standing waves in the Hifi Spectrum. The fitBaseline task, which is a routine to fit and subtract or divide baselines in the HIFI spectra, was used in the subtract setting. Following the processing and reduction of the observations we exported the observations from HIPE in ascii format.

2.1.2 IRAF & Post IRAF Reduction & Analysis

The ascii files were converted from the redshifted frequency to the rest frame wavelength and read into IRAF for spectral analysis. Once in IRAF any exposures that overlapped were combined to enhance the signal-to-noise ratio. These combined spectra were then were then normalized to the continuum level, using the IRAF CONTINUUM task.

We searched for a total of 36 lines: CN 794 GHz, 9067 GHz, 1133.2 GHz, 1133.0 GHz; CO 807 GHz, 922 GHz, 1152 GHz, 1267 GHz, 1382 GHz, 1497 GHz; ^{13}CO 771 GHz, 881 GHz; C^{18}O 768 GHz, 878 GHz, 1097 GHz, 1207 GHz, 1316 GHz, 1426 GHz; H_2O 752 GHz, 1113 GHz; NH 946 GHz; HCO 766.9961304 GHz, 767.0888059 GHz, 779.0257538 GHz, 779.0321584 GHz, 779.1463894 GHz, 779.1527554 GHz, 792.5329087 GHz, 792.5419253 GHz, 792.6951114 GHz, 792.70416 GHz; C I 809 GHz; [C II] 1901 GHz; [N II] 1460 GHz; and CH+ 835 GHz. For these lines, if there was any sign of a line at the wavelength, we measured the equivalent width using the program specp. Using the Eq. 2.1 we obtained the significance of the detection.

$$\sigma = \frac{W}{\delta W} = \frac{W}{(\Delta\lambda/SNR)\sqrt{\#of Pixels}} \tag{2.1}$$

In Eq. 2.1, W is the measured equivalent width, SNR is the measured signal to noise per pixel, $\Delta\lambda$ is the dispersion (wavelength step per pixel), and the "$\#ofpixels$" is the number of pixels occupied by the line. After the normalization of the data, the spectra were exported to ascii format using the task wspectext.

For lines with a 3σ detection, we used a script to numerically calculate the integrated optical depth, Eq. 2.2 (Neufeld et al., 2010).

$$\int \tau_V dV = \int \ln \frac{F_{continuum}}{F_V} dV \tag{2.2}$$

In Eqs. 2.2, $F_{continuum}$ is the measured continuum flux. The integration is covered over the extent of the detected line. We then proceeded to calculate the column density, N, of the molecule or ion using Eq. 2.3 (Neufeld et al., 2010).

$$\int \tau d\nu = \frac{A_{ul} g_u \lambda^3}{8\pi g_l} N \tag{2.3}$$

Here, λ correspond to the central wavelength, g_l and g_u are the Landé g-factors (ie. lower and upper statistical weights, where $g = 2J + 1$.), and A_{ul} is the spontaneous transition probability. The necessary A_{ul}, g_u, and g_l values are from *NIST Atomic Spectra Database (ver. 5.1)*, Pickett et al., 1998, and Müller et al., 2005.

2.2 RESULTS

For 3 of the 5 absorption systems we had tentative detections of molecular lines of 3 sigma or greater as shown in Table 2.2. We had a large number of non-detections

Table 2.2 Summary of Herschel Searches for Molecular Absorption

PKS0420-014				
Line	$\int \tau_V$ dV (km/s)	W (Å)	log N	V$_c$(km/s)
CO 216	≤19.85	≤395.98	≤17.02	89.93
C^{18}O 227	≤29.35	≤555.27	≤17.00	-279.67
C^{18}O 248	92.70±4.17	513.59±145.32	17.38±0.11	-178.32
[C II 1901]	≤20.31	≤384.43	≤19.47	-23.89

PKS2355-106				
Line	$\int \tau_V$ dV (km/s)	W (Å)	log N	V$_c$(km/s)
CO 200	≤62.34	≤1143.92	≤17.50	170.36

AO0235+164				
Line	$\int \tau_V$ dV (km/s)	W (Å)	log N	V$_c$(km/s)
HCO 792.70	≤0.10	≤9.91	≤13.20	-0.32
C^{18}O 248	648.75±46.78	4543.04±1102.15	18.02±0.09	-173.66

PKS1830-211				
Line	$\int \tau_V$ dV (km/s)	W (Å)	log N	V$_c$(km/s)
[N II 1460]	≤38.30	≤691.40	≤19.33	-112.81

TXS0827+243				
Line	$\int \tau_V$ dV (km/s)	W (Å)	log N	V$_c$(km/s)
HCO 792.70	1.21±0.06	15.09±4.83	13.25±0.12	-0.25
C^{18}O 273	≤25.45	≤775.47	≤17.06	91.76

due to limited signal to noise for which we were able to place 3σ upper limits on equivalent width, integrated optical depth, and column densities.

The absorber in the direction of PKS0420-014 at $z_{\rm abs}$=0.633 showed 1 tentative detection, C^{18}O 248, which was detected at the 3.75σ level. This line at V$_{\rm c}$=-178.32 km/s gives a log N value of 17.07 ± 0.11. In addition there were 3 other covered lines that showed visible features that are displayed in figure 2.1. These addition lines were not detected at the 3σ level. One of the lines, C^{18}O 227, was seen at the 2.80σ level, which agrees with relative line strengths for the two C^{18}O transitions.

The absorber in the direction of PKS2355-106 at $z_{\rm abs}$=1.17260 did not show any lines at the 3σ detection limit. However figure 2.2 shows the 1 line with any visible feature.

The absorber in the direction of AO0235+164 at $z_{\rm abs}$=0.52385 showed 1 detection, C^{18}O 248, at the 4.12σ level. Figure 2.3, shows this line and the upper limit line,

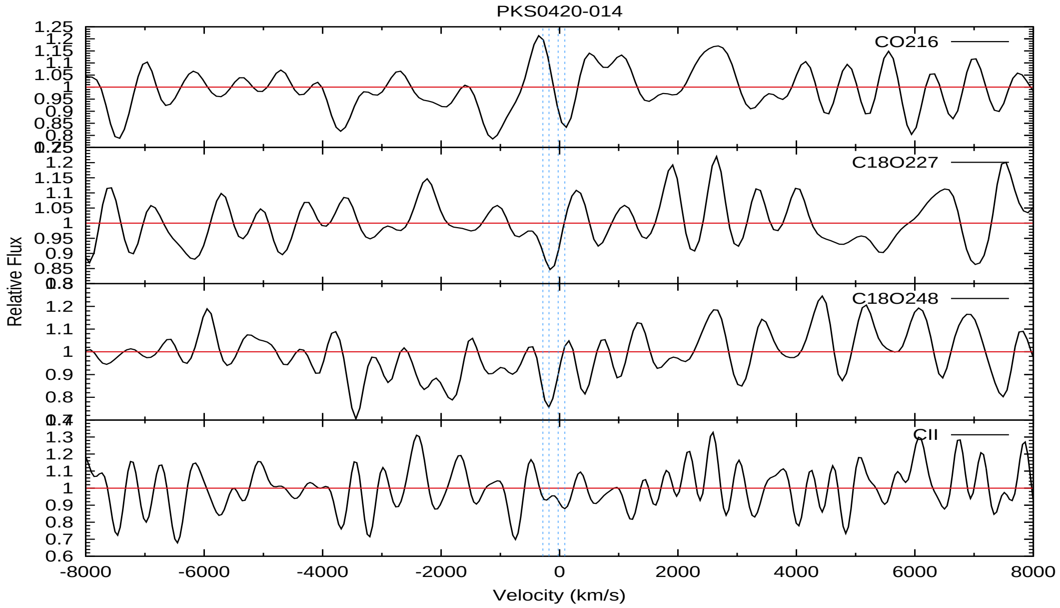

Figure 2.1 Molecular absorption at $z_{abs} = 0.633$ of PKS0420-014.

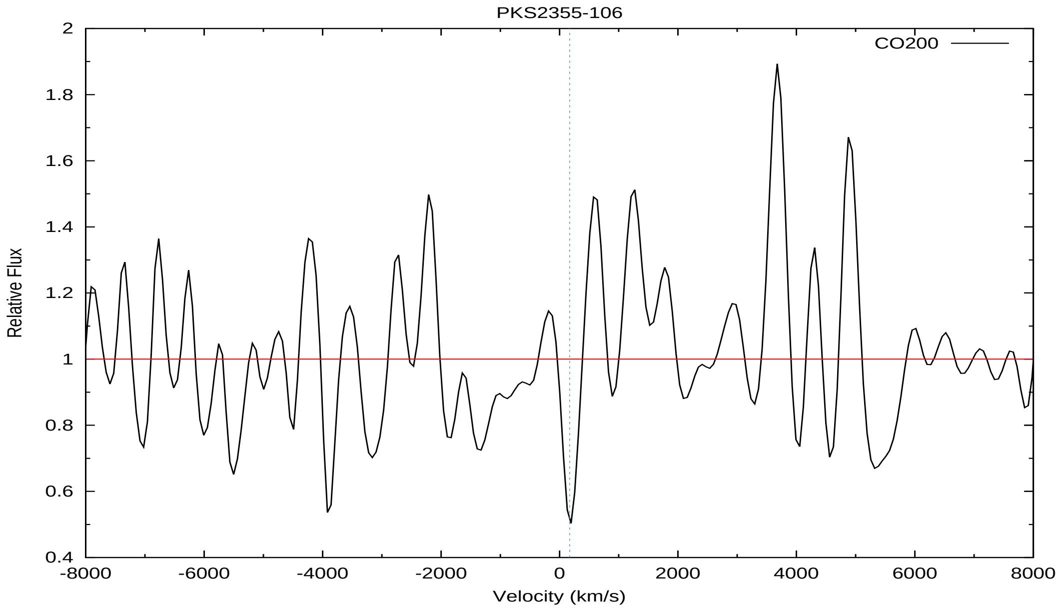

Figure 2.2 Molecular absorption at $z_{abs} = 1.17260$ of PKS2355-106.

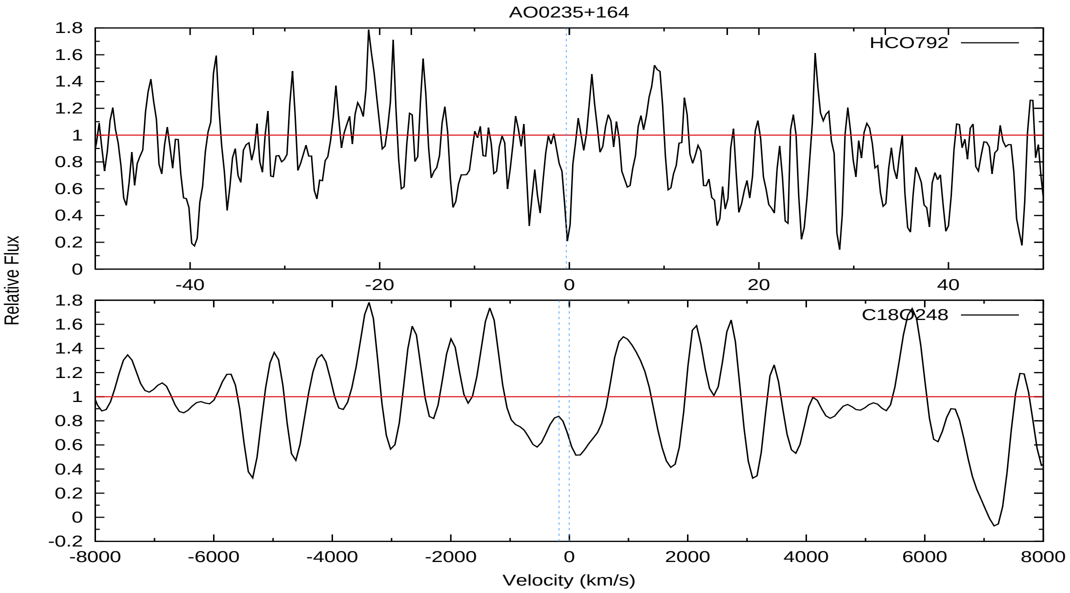

Figure 2.3 Molecular absorption at $z_{abs} = 0.52385$ of AO0235+164.

HCO 792.70.

Figure 2.4 shows the 1 line that had any visible feature in the direction of PKS1830-211 at $\mathrm{z_{abs}}$=0.88583. In this system, there was no detection at the 3σ level.

The absorber in the direction of TXS0827+243 at $\mathrm{z_{abs}}$=0.52476 showd one line, HCO 792.70, at the 3.12σ level. Figure 2.5 shows this line in addition to a upper limit line of $\mathrm{C^{18}O}$ 273.

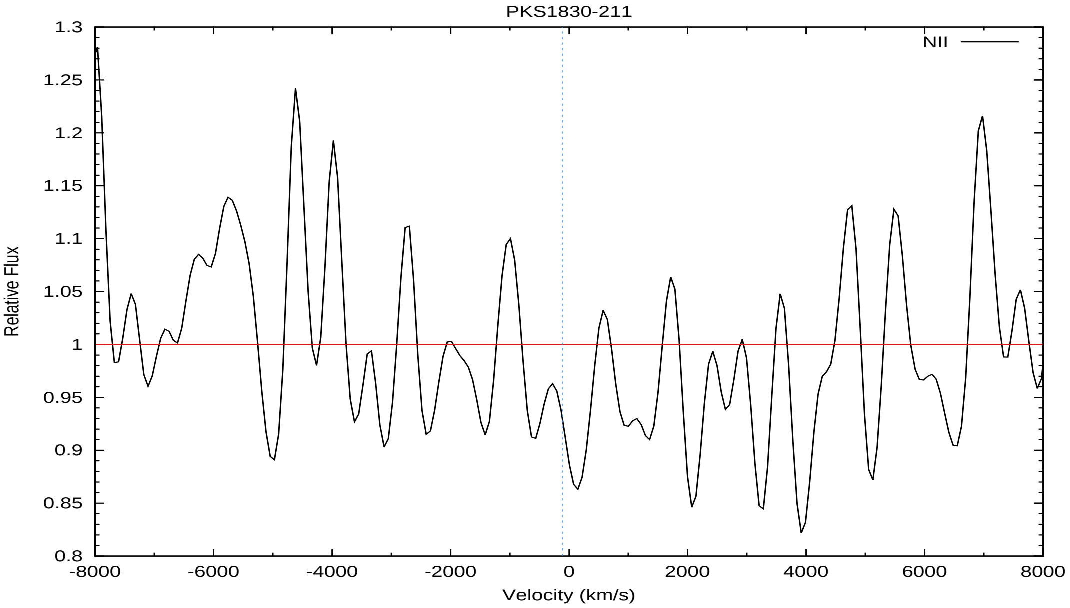

Figure 2.4 Molecular absorption at $z_{abs} = 0.88583$ of PKS1830-211.

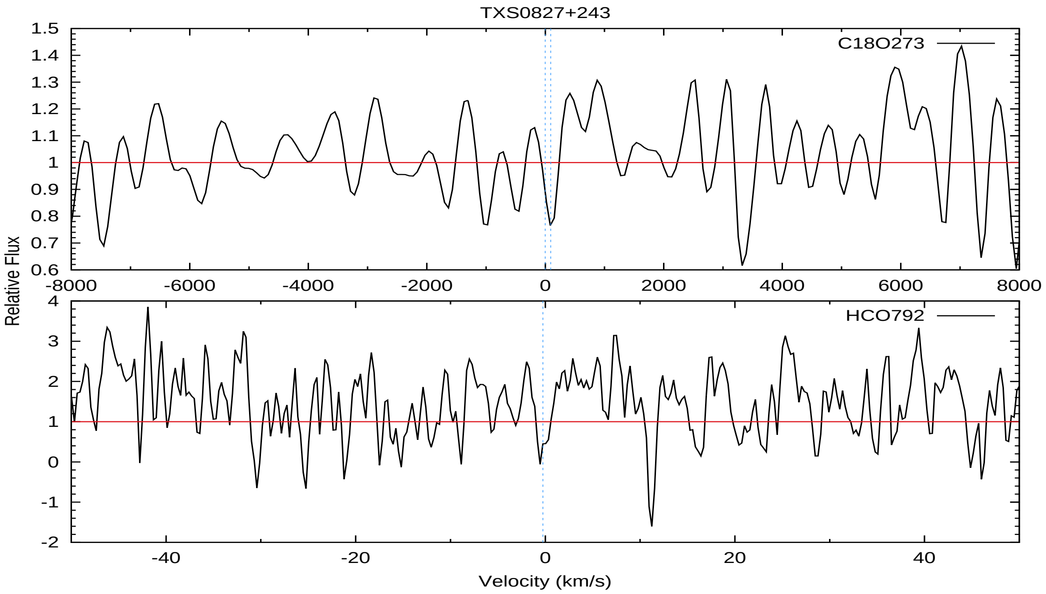

Figure 2.5 Molecular absorption at $z_{abs} = 0.52476$ of TXS0827+243.

CHAPTER 3

METAL & MOLECULAR ABSORPTION IN SUPER-DLAS

Here we present optical spectroscopy aimed at the study of metals and molecules in two super-DLA absorbers, and compare the results for these absorbers to those for DLAs from the literature. The results presented here appear in Kulkarni et al., 2015 (ApJ, in press).

3.1 OBSERVATIONS AND DATA REDUCTION

The Super-DLAs observed in this study, shown in table 3.1, were selected because their SDSS spectra showed Lyman-α absorption of log $N_{HI} \geq 21.7$ and the presence of several metal lines (Noterdaeme et al., 2014). We obtained follow-up higher spectral resolution spectra using Keck Echellette Spectrograph and Imager (ESI; Scheinis et al., 2002) of the quasars with the goal of determining accurate element abundances measurements.

Table 3.1 Super-DLAs Observed with Keck ESI

Quasar	RA,DEC(J2000)	z_{em}	z_{abs}	Instrument	Integration time
Q0230-0334	02:30:11.30-03:34:50.2	2.872	2.5036	Keck/ESI	2100s×1
Q0743+1421	07:43:44.26+14:21:34.9	2.281	2.045	Keck/ESI	1800s×2+1300s

These spectra were obtained in classical mode on November 7-8, 2013 under NOAO program 2013B-0525 (PI: V.Kulkarni) where losses due to weather problems (of 1.8 nights out of 2 awarded) allowed us to obtain only one exposure for Q0230-0334 and three exposures for Q0743+1421. The spectra were reduced and extracted using ESIRedux, an IDL-based reduction package written by J. X. Prochaska. The extracted spectra from individual orders were split on average into 3 pieces (typically $\sim 100 - 400$ Å wide), which were continuum-fitted using the IRAF "CONTINUUM" task. We tried both cubic spline and Legendre polynomials, typically of order $3 - 5$, to fit the continuum and used the function which provided the best fit as judged from the RMS of the residuals. For the absorber towards J0743+1241, the continuum-normalized pieces from the 3 exposures were combined into a single piece for each wavelength range using the IRAF "SCOMBINE" task.

3.1.1 ABSORPTION LINE MEASUREMENTS

The absorption lines were fit by Voigt profiles (see Appendix D) using the program VPFIT[1] version 10.0 to determine the relative column densities. Figures 3.1 and 3.2 show the Voigt profile fits of the H I Lyman-α lines for the super-DLAs towards Q0230-0334 and Q0743+1421 respectively. For Q0743+1421, the spectra obtained from ESI did not cover the Lyman-α absorption line of the super-DLA absorber; therefore the relevant region of the SDSS DR12 BOSS spectra was fitted to measure the N_{HI} for this super-DLA, using a 7th order Chebyshev function for continuum fitting (Fig. 3.2). Figs. 3.3 - 3.4 and 3.5 - 3.7 correspondingly show the profile fits to key metal lines for Q0230-0334 and Q0743+1421.

For Q0230-0334, which had multiple velocity components, the total column density was obtained by summing over the individual components. In all unsaturated and unblended cases, the determined column densities were checked against the independently determined values from the apparent optical depth method (AOD; see Savage and Sembach, 1991 or Appendix E). For these fits, we have adopted oscillator strengths from Morton (2003) and Solar abundances from Asplund et al. (2009).

---

[1] http://www.ast.cam.ac.uk/rfc/vpfit.htm

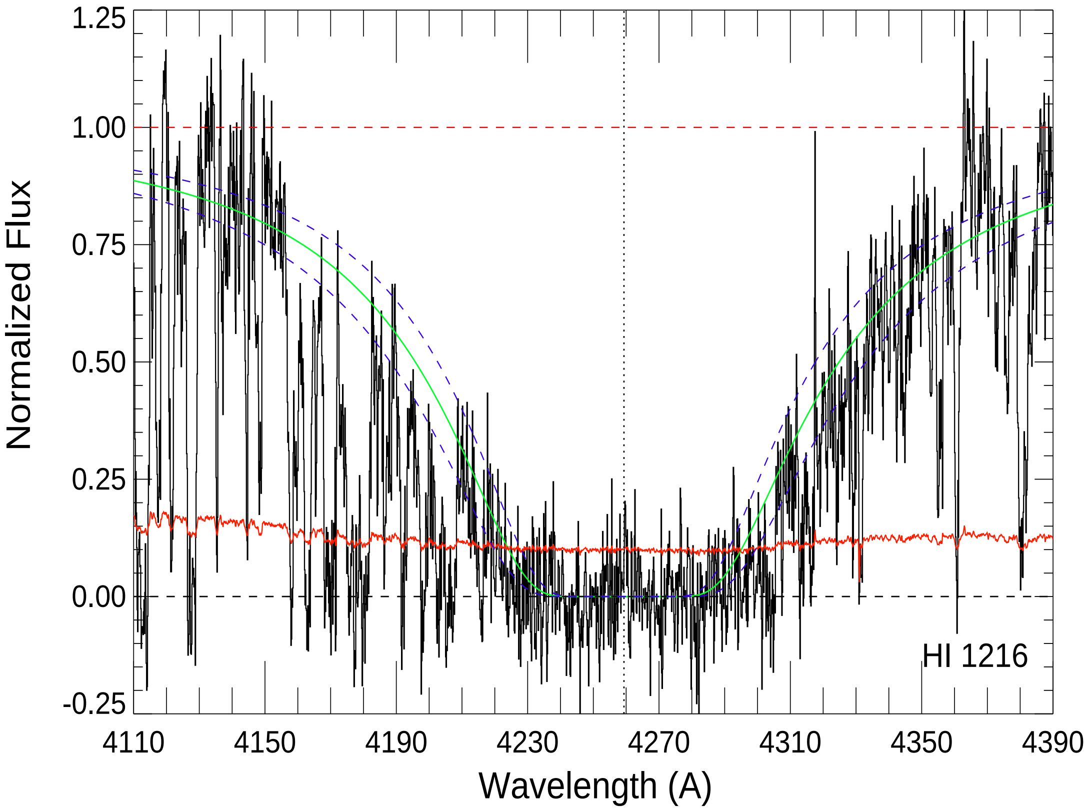

Figure 3.1 H I Lyman-α absorption feature in our ESI data for the $z = 2.5036$ absorber towards Q0230-0334. The continuum-normalized flux is shown in black, while the 1σ error array in the normalized flux is shown in red. The solid green curve represents the best-fitting Voight profile corresponding to log $N_{HI} = 21.74$ and the dashed blue curves denote the profiles corresponding to the estimated $\pm1\sigma$ deviations (±0.1 dex) from the best-fitting N_{HI} value. The horizontal dashed red line denotes the continuum level. The vertical dotted black line denotes the center of the Lyman-α line.

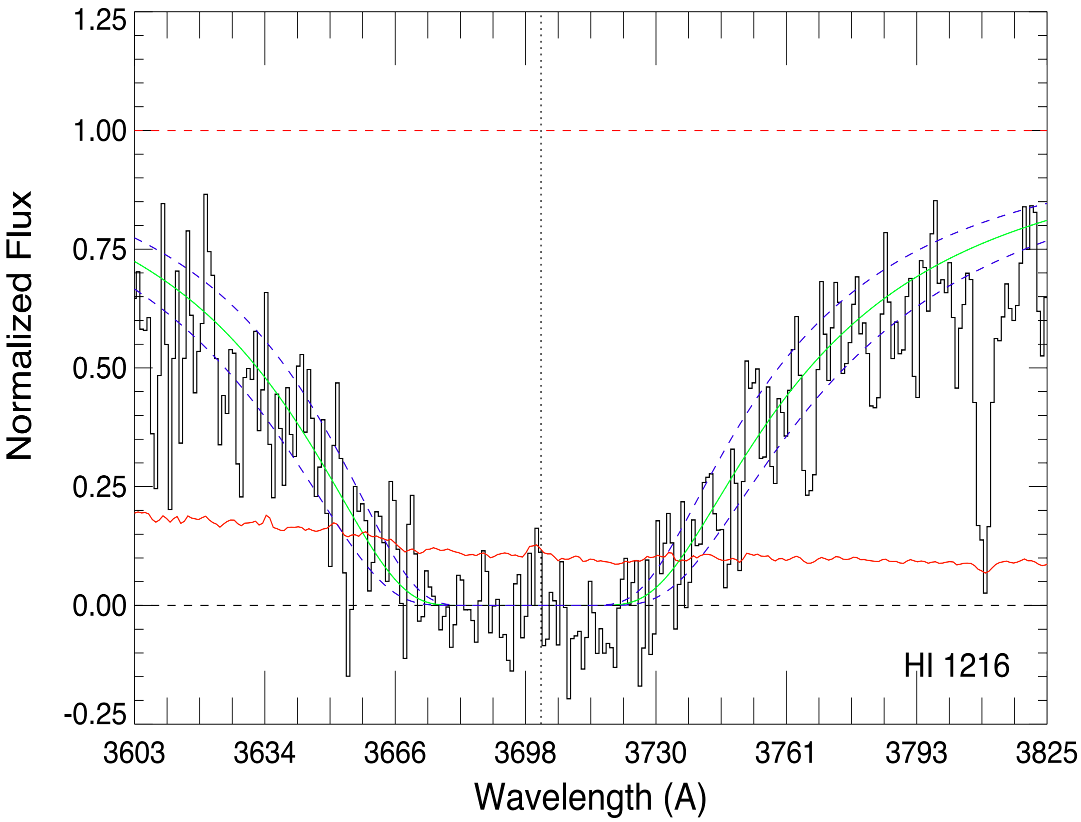

Figure 3.2 Same as Figure 3.1, but for the $z = 2.045$ super-DLA towards Q0743+1421. The solid green an dashed blue profiles correspond to log $N_{HI} = 21.9 \pm 0.1$.

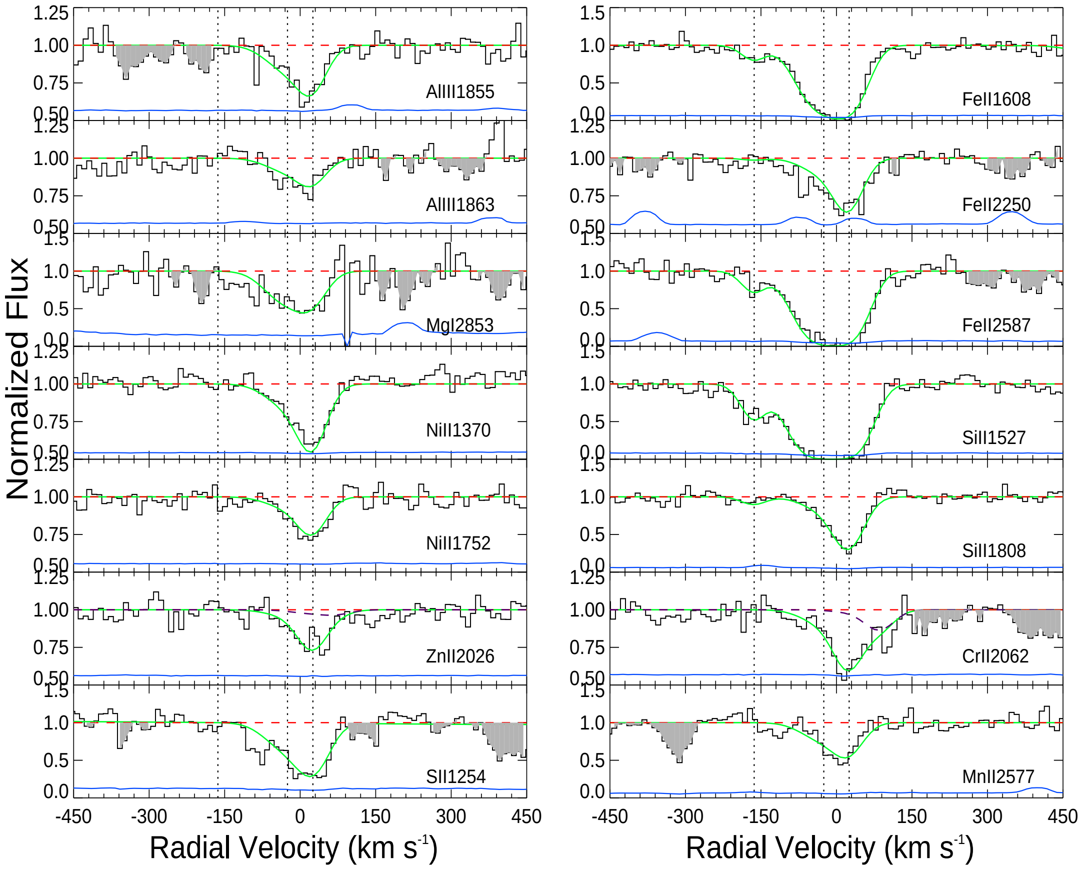

Figure 3.3 Velocity plots for several metal lines of interest for the $z = 2.5036$ system in the spectrum of Q0230-0334. In each panel, the normalized data are shown in black, the solid green curve indicates the theoretical Voigt profile fit to the absorption feature, and the dashed red line shows the continuum level. The 1σ error values in the normalized flux are represented by the blue curves near the bottom of each panel. Note that in a few panels with weak lines, if the normalized flux scale shown starts at 0.5, the 1-σ error arrays have been offset by 0.5, so that they can be viewed in the same panels. The vertical dotted lines indicate the positions of the components that were used in the fit. In the 'ZnII 2026' panel, the solid green curve represents the combined contributions from Zn II λ 2026.1 and Mg I λ 2026.5 lines while the contribution from Mg I λ 2026.5 alone to this blend, determined from the Mg I λ 2853 line, is represented by the dashed purple curve. The solid green curve in the 'CrII 2062' panel represents the combined contributions from Cr II λ 2062.2 and Zn II λ 2062.7 lines and the contribution from the Zn II λ 2062.7 line alone is shown using a dashed purple line. The regions shaded in gray in some of the panels represent absorption unrelated to the line presented or regions of high noise.

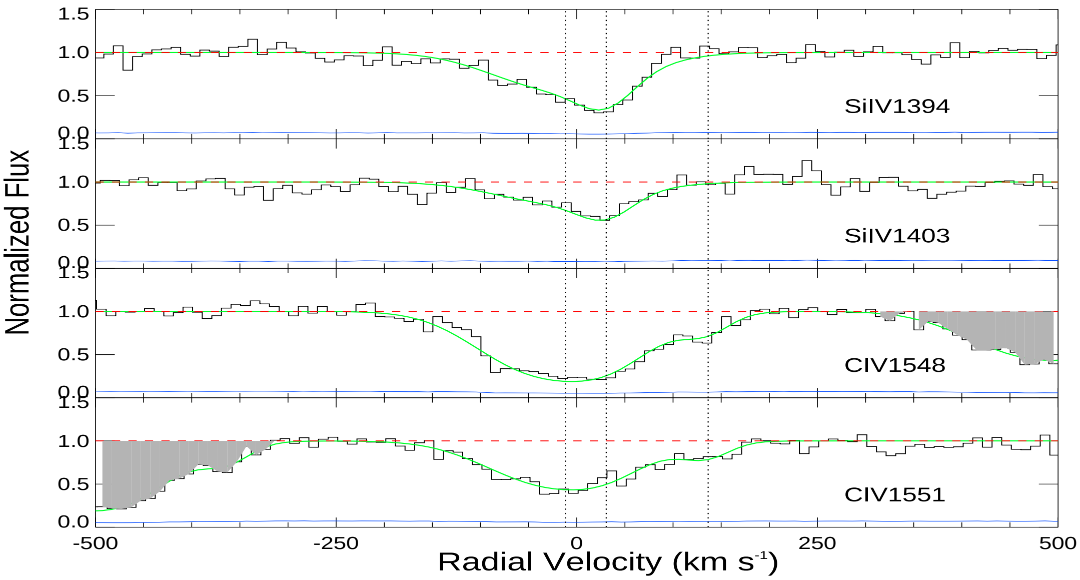

Figure 3.4 Same as Figure 3.3, but for the high-ionization metal absorption lines in the $z = 2.5036$ super-DLA toward Q0230-0334.

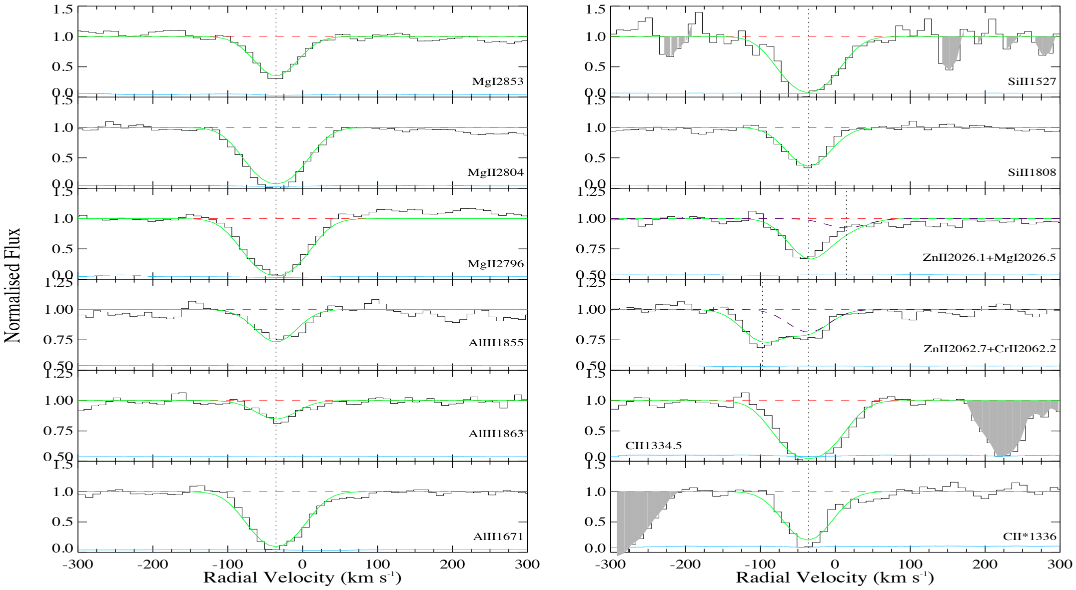

Figure 3.5 Same as Figure 3.3, but for key low-ionization metal absorption lines in the $z_{abs} = 2.045$ super-DLA toward Q0743+1421.

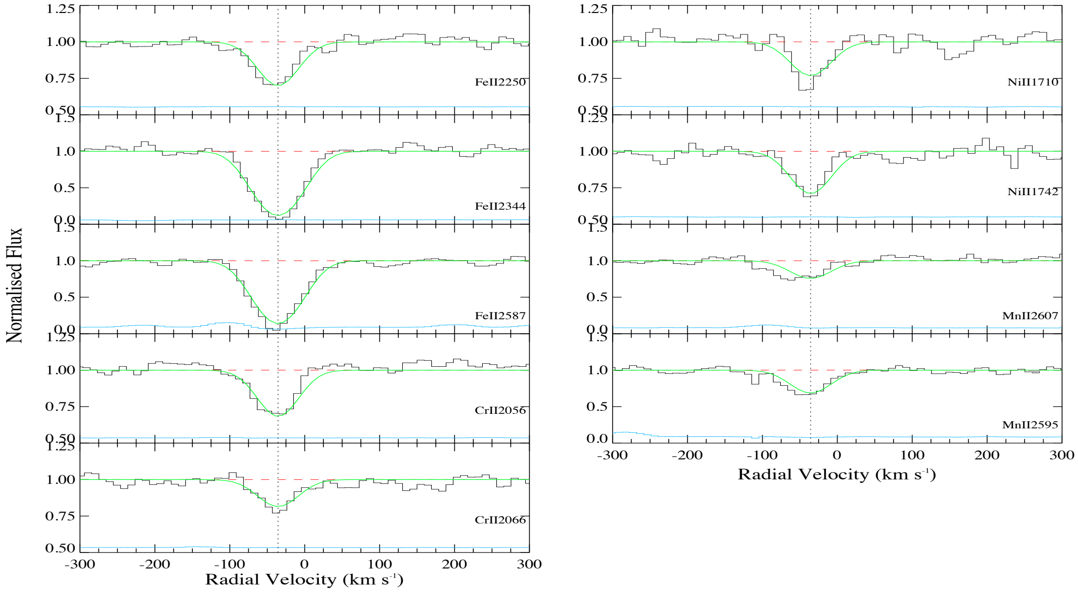

Figure 3.6 Same as Figure 3.3, but for additional low-ionization metal absorption lines in the $z_{abs} = 2.045$ super-DLA toward Q0743+1421.

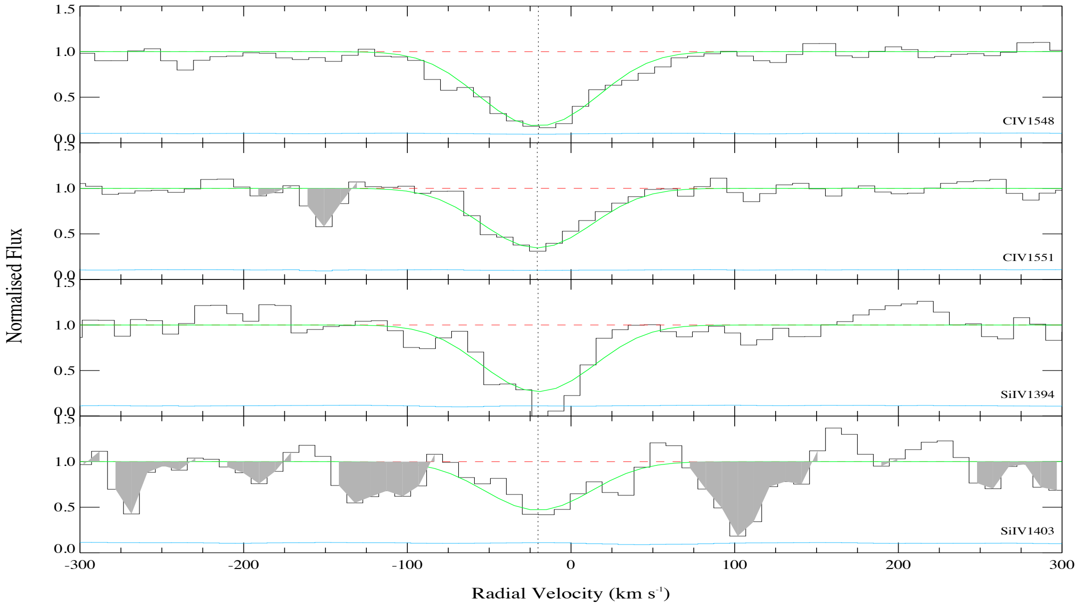

Figure 3.7 Same as Figure 3.3, but for the high-ionization lines in the $z_{abs} = 2.045$ super-DLA toward Q0743+1421.

Table 3.2 Results of Voigt profile fitting for lower ions in the $z = 2.5036$ absorber toward J0230-0334

z	b^1_{eff}	$\log N_{\rm MgI}$	$\log N_{\rm FeII}$	$\log N_{\rm ZnII}$	$\log N_{\rm NiII}$	$\log N_{\rm CrII}$
2.50167 ± 0.00002	7.6 ± 0.7	...	13.86 ± 0.07	...	...	...
2.50329 ± 0.00014	45.6 ± 6.3	12.61 ± 0.14	14.99 ± 0.15	12.13 ± 0.41	13.75 ± 0.14	13.38 ± 0.21
2.50388 ± 0.00002	22.1 ± 2.0	12.44 ± 0.22	15.45 ± 0.07	12.88 ± 0.07	14.18 ± 0.05	13.92 ± 0.07

z	b^1_{eff}	$\log N_{\rm SiII}$	$\log N_{\rm SII}$	$\log N_{\rm MnII}$	$\log N_{\rm AlIII}$
2.50167 ± 0.00002	7.6 ± 0.7	14.88 ± 0.20	...	...	...
2.50329 ± 0.00014	45.6 ± 6.3	15.26 ± 0.15	15.17 ± 0.08	13.04 ± 0.08	12.82 ± 0.14
2.50388 ± 0.00002	22.1 ± 2.0	16.06 ± 0.05	15.68 ± 0.14	13.20 ± 0.07	12.95 ± 0.11

---

[1] b_{eff} denotes the effective Doppler b parameter in km s^{-1}. Logarithmic column densities are in cm^{-2}.

Table 3.3 Results of Voigt profile fitting for higher ions in the $z = 2.5036$ absorber toward J0230-0334

z	b^1_{eff}	$\log N_{\mathrm{CIV}}$	$\log N_{\mathrm{SiIV}}$
2.50345 ± 0.00004	84.8 ± 2.8	14.53 ± 0.02	13.70 ± 0.04
2.50394 ± 0.00004	18.4 ± 9.1	13.12 ± 0.48	13.45 ± 0.08
2.50518 ± 0.00005	5.4 ± 1.8	13.70 ± 0.33	...

---

[1] b_{eff} denotes the effective Doppler b parameter in km s^{-1}. Logarithmic column densities are in cm^{-2}.

Table 3.4 Total column densities for the $z = 2.5036$ absorber toward J0230-0334

Ion	log N^{fit} (cm^{-2})	log N^{AOD} (cm^{-2})
H I	21.74 ± 0.10	...
C IV	14.60 ± 0.05	14.59 ± 0.01
B II	...	< 11.78
Mg I	12.83 ± 0.12	12.85 ± 0.05
Al III	13.19 ± 0.08	13.14 ± 0.06
Si II	16.15 ± 0.04	15.96 ± 0.02
Si II*	...	< 12.85
Si IV	13.89 ± 0.04	13.86 ± 0.03
S II	15.80 ± 0.11	15.72 ± 0.02
Ti II	...	< 12.83
V II	...	< 12.83
Cr II	14.03 ± 0.07	...
Mn II	13.43 ± 0.05	13.36 ± 0.03
Fe II	15.59 ± 0.06	15.64 ± 0.03
Co II	...	< 13.23
Ni II	14.32 ± 0.05	14.32 ± 0.03
Cu II	...	< 12.33
Zn II	12.95 ± 0.09	...
Ge II	...	< 12.82

Table 3.5 Measured element abundances relative to solar for the $z = 2.5036$ absorber toward J0230-0334

Element	[X/H][1]
B	< -0.66
Si	-1.10 ± 0.11
S	-1.06 ± 0.15
Ti	< -1.86
V	< -0.84
Cr	-1.35 ± 0.12
Mn	-1.74 ± 0.11
Fe	-1.65 ± 0.12
Co	< -1.50
Ni	-1.64 ± 0.11
Cu	< -1.60
Zn	-1.35 ± 0.13
Ge	< -0.57

---

[1] Abundance estimates based on the dominant metal ionization state and H I.

Table 3.6 Results of Voigt profile fitting for lower ions in the $z = 2.045$ absorber toward Q0743+1421

z	b^1_{eff}	N_{AlII}	N_{AlIII}	N_{CII}	$N_{\text{CII*}}$	N_{CrII}	N_{FeII}
2.04464 ± 0.000003	17.799 ± 0.378	> 14.671	12.933 ± 0.0326	> 16.906	> 14.961	13.723 ± 0.0213	15.403 ± 0.0449

z	b^1_{eff}	N_{MgI}	N_{MgII}	N_{MnII}	N_{NiII}	N_{SiII}	N_{ZnII}
2.04464 ± 0.000003	17.799 ± 0.378	12.968 ± 0.0385	> 15.590	13.180 ± 0.0454	14.123 ± 0.0300	> 16.083	13.048 ± 0.0268

---

[1] b_{eff} denotes the effective Doppler b parameter in km s^{-1}. Logarithmic column densities are in cm^{-2}.

Table 3.7 Results of Voigt profile fitting for higher ions in the $z = 2.045$ sub-DLA toward Q0743+1421

z	b^1_{eff}	N_{CIV}	N_{SiIV}
2.0440 ± 0.000016	26.432 ± 2.740	14.407 ± 0.0708	13.845 ± 0.0574

---

[1] b_{eff} denotes the effective Doppler b parameter in km s^{-1}. Logarithmic column densities are in cm^{-2}.

Table 3.8 Total Column Densities for the $z = 2.045$ Absorber toward Q0743+1421

Ion	log N^{fit} (cm^{-2})	log N^{AOD} (cm^{-2})
H I	21.90 ± 0.10	...
C I	...	< 13.08
C II	> 16.91	> 14.82
C II*	> 14.96	> 14.46
C IV	14.41 ± 0.07	14.21 ± 0.03
B II	...	< 12.26
Mg I	12.97 ± 0.04	12.71 ± 0.02
Mg II	> 15.59	> 13.57
Al II	> 14.67	> 13.35
Al III	12.93 ± 0.03	12.82 ± 0.04
Si II	> 16.08	> 15.76
Si II*	...	< 13.01
Si IV	13.84 ± 0.06	13.76 ± 0.06
V II	...	< 12.79
Cr II	13.72 ± 0.02	13.62 ± 0.02
Mn II	13.18 ± 0.05	13.04 ± 0.03
Fe II	15.40 ± 0.04	15.46 ± 0.06
Co II	...	< 13.67
Ni II	14.12 ± 0.03	14.20 ± 0.04
CuII	...	< 12.90
Zn II	13.05 ± 0.03	...
Ga II	...	< 12.07
Ge II	...	< 12.88

Table 3.9 Measured Element Abundances Relative to Solar for the $z = 2.045$ Absorber toward Q0743+1421

Element	[X/H][1]
C	> -3.51
B	< -0.3
Mg	> -3.93
Al	> -3.00
Si	> -1.65
V	< -1.0
Cr	-1.82 ± 0.10
Mn	-2.15 ± 0.11
Fe	-2.00 ± 0.11
Co	...
Ni	-2.00 ± 0.10
Cu	< -1.2
Zn	-1.41 ± 0.10
Ga	< -0.9
Ge	< -0.7

---

[1] Abundance estimates based on the dominant metal ionization state and H I.

3.2 Results of Profile Fitting and Column Density Measurements

Tables 3.2 and 3.3 list the measurements of metal column densities for the absorber toward Q0230-0334, while tables 3.6 and 3.7 list the metal column density measurements for the absorber toward Q0743+1421. Tables 3.4 and 3.8 give the total column densities (summed over individual velocity components) derived from the profile fits, along with the AOD estimates, if available, for Q0230-0334 and Q0743+1421, respectively, while tables 3.5 and 3.9 list the corresponding element abundances, calculated using the total metal column densities along with the H I column density, and using the solar abundances from Asplund et al. (2009). For these systems, due to the high N_{HI}, ionization corrections would be negligible, so therefore are not calculated.

3.3 Discussion

3.3.1 Element Abundances and Dust Depletions

The DLAs towards Q0230-0334 and Q0743+1421 both show Zn abundances in the narrow range with [Zn/H] $= -1.35$ and [Zn/H] $= -1.41$ dex respectively. In addition, the super-DLAs towards Q0230-0334 and Q0743+1421 show [Fe/Zn] $= -0.30$ and -0.59 dex respectively, and [Ni/Zn] $= -0.29$ and -0.59 dex respectively. Meanwhile, Mn is even less abundant relative to Zn at [Mn/Zn] $= -0.39$ and -0.74 dex respectively for Q0230-0334 and Q0743+1421. For the absorber towards Q0230-0334, Cr appears to be weakly depleted at [Cr/Zn] $= 0.0 \pm 0.11$, which seems surprising. While the absorber towards Q0743+1421 shows a higher depletion of [Cr/Zn] $= -0.41 \pm 0.04$.

Another potentially interesting feature of the relative abundance patterns is that in one out of the two super-DLAs studied here, Si is observed to be more abundant relative to Zn than in the Sun, with [Si/Zn] of 0.25 ± 0.10 dex relative to the Sun.

S, which shows nearly zero depletion in the Galactic interstellar medium (ISM;

Savage and Sembach, 1996), is a better indicator of the abundance of the α elements then Si (which is depleted by $\sim 0.3 - 0.4$ dex even in the warm Galactic ISM; e.g., Savage and Sembach, 1996; Jenkins, 2009). It is therefore interesting to note that, in the only system for which we have a S measurement, S is also more abundant relative to Zn than in the Sun with the S/Zn ratio of 2.85 dex for the super-DLA towards Q0230-0334, which gives a ratio higher by 0.29 ± 0.20 compared to the solar ratios. However, the S/Si is somewhat higher than solar at -0.35 dex (higher by 0.04 ± 0.12 dex).

The large [S/Zn] and [Si/Zn] values for Q0230-0334 suggests that Zn does not behave like an α element, while the large [S/Fe] value suggests α-enhancement and some dust depletion.

3.3.2 SEARCH FOR RARE METALS

Due to the high N_{HI}, Super-DLAs offer an excellent opportunity to study the abundances of rare elements. Observations of such rare elements can offer additional constrains on nucleosynthetic processes in the absorbing galaxies. For example, V and Co are believed to be produced mainly in explosive Si burning in type II supernovae and to a smaller extent in type Ia supernovae (e.g., Woosley and Weaver, 1995; Bravo and Martinex-Pinedo, 2012; Battistini and Bensby, 2015).

For the super-DLAs toward Q0230-0334 and Q0743+1421, no absorption lines of the rare elements such as B, V, Co, Cu, Ge, and Ga were detected. However, 3σ upper limits were determined using the AOD method and are listed as such in Tables 3.4 and 3.8 with their corresponding abundance limits in Tables 3.5 and 3.9

The absorber toward Q0230-0334 shows an under-abundance of Cu, with [Cu/Zn] <-0.25, while for the absorbers toward Q0743+1421 the limits are less constraining with [Cu/Zn] <0.21. The absorber towards Q0230-0334, the only system for which we have Co measurements, shows [Co/Zn] <-0.15. Higher S/N observations are necessary to obtain more definitive abundances of these rare elements.

3.3.3 Comparison with Other DLAs

In order to compare the super-DLAs (log $N_{HI} \leq 21.7$), including those towards Q0230-0334 and Q0743+1421, with DLAs ($20.3 \leq$ log $N_{HI} \leq 21.7$), our super-DLAs were combined with 11 other super-DLAs from literature that have element abundances based on moderate or high-resolution spectra (typically $R > 6000$)(Prochaska et al., 2003; Heinmuller et al., 2006; Noterdaeme et al., 2007; Noterdaeme et al., 2008; Noterdaeme et al., 2015a; Kulkarni et al., 2012; Guimaraes et al., 2012; Ellison et al., 2012; Berg et al., 2015).

The current sample of DLAs exhibits a deficit of absorbers with high N_{HI} and high metallicity. It has been suggested by Boissé et al. (1998) that this could be the result of a dust selection effect, where high-N_{HI} systems with high-metallicity could be more dusty causing the background quasars to be obscured, thus leading to a systematic under-representation in the high-resolution spectroscopic studies. However it could be the result of Hydrogen becoming predominantly molecular above some metallicity dependent N_{HI} threshold (Schaye, 2001; Krumholz et al., 2009a).

Fig. 3.8 compares the metallicity vs. H I column density data for DLAs and super-DLAs with detections of Zn or S toward quasars and GRB afterglows. The red filled circles and blue unfilled triangles show the measurements for quasar super-DLAs from our work and those from the literature. The black unfilled squares denote the measurements for other quasar DLAs with log $N_{\mathrm{HI}} < 21.7$ (from many references such as Ledoux et al. (2006), Péroux et al. (2006), Meiring et al. (2006), Prochaska et al. (2001), Prochaska et al. (2007), Noterdaeme et al. (2008), Rafelski et al. (2012), Rafelski et al. (2014); see Kulkarni et al. (2007), Kulkarni et al. (2010), and Som et al. (2015) for further details). The orange and green diamonds denote the measurements for DLAs and super-DLAs toward GRB afterglows. The GRB data are from Vreeswijk

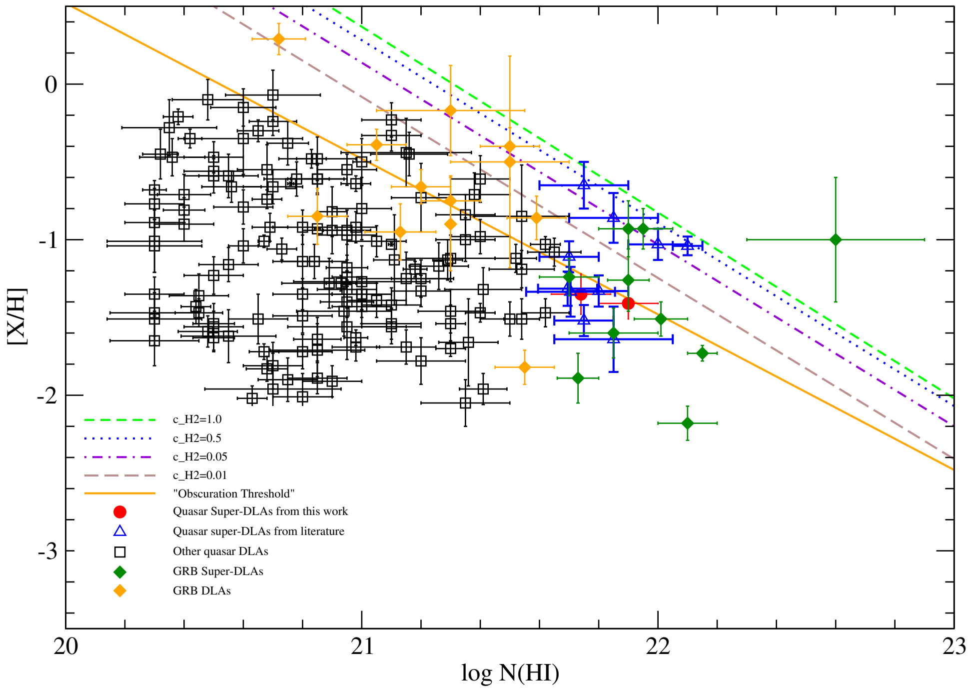

Figure 3.8 Plot of metallicity (based on Zn or S absorption) vs. H I column density for quasar super-DLAs from this study and the literature, other quasar DLAs, and GRB DLAs/ super-DLAs. Short-dashed, dotted, dot-dashed, and long-dashed curves show trends expected for molecular Hydrogen core “covering fractions" of 1.0, 0.5, 0.05, and 0.01, adopted from Krumholz et al. (2009a). The solid orange line shows the “obscuration threshold” of Boissé et al. (1998).

et al. (2004), Prochaska et al. (2007), Ledoux et al. (2009), Savaglio et al. (2012), Cucchiara et al. (2015), and references therein. The GRB DLAs and super-DLAs are at the GRB redshifts and are thus associated with the GRB host galaxies. [We note that, while we have used the $N_{\rm HI}$ reported in these studies for the GRB DLAs, the H I behind the GRB is not sampled by the GRB DLA sightlines, since the GRB is located within the host galaxy. Thus the true $N_{\rm HI}$ for the GRB sightlines may be expected to be higher by a factor of 2 (i.e., 0.3 dex) on average. The total metal columns along those sightlines may also be proportionately larger, and so the metallicities may not be that different.] We show in solid orange the line [X/H]=20.59$-$log $N_{\rm HI}$ corresponding to the "obscuration threshold" that was suggested by Boissé et al. (1998) as a potential way to explain the deficit of DLAs with large $N_{\rm HI}$ and high metallicity.

The short-dashed (green), dotted (blue), dot-dashed (violet), and long-dashed (brown) lines in Fig. 3.8 show the curves calculated by Krumholz et al. (2009a) for "covering" fractions $c_{\rm H_2}$ = 0.01, 0.05, 0.5, and 1.0 for the cross-section of the spherical molecular core of the cloud (surrounded by a shell of atomic gas). These $c_{\rm H_2}$ values correspond to molecular mass fractions $f_{\rm H_2} = M_{\rm H_2}/M_{\rm total} = [1 - \{(1 - c_{\rm H_2}^{-1.5})/\phi_{mol}\}]^{-1}$ = 0.010, 0.102, 0.845, and 1.0, respectively. [The quantity ϕ_{mol} is the ratio of molecular gas density to atomic gas density, and is about 10 (Krumholz, McKee, and Tumlinson, 2009b)].

Several interesting facts emerge from Fig. 3.8: (1) A fraction of ∼46% of the quasar super-DLAs lie on or above the "obscuration threshold", while only ∼9% of the quasar DLAs lie on or above that threshold. About 77% of the quasar super-DLAs lie above or within 1σ of the obscuration threshold (including both of the super-DLAs studied here), while only ∼15% of the quasar DLAs do so. For GRB absorbers, the super-DLA and DLA fractions above or within 1σ of the threshold are more comparable, ∼ 75% and 60%, respectively. (We note that the fractions of GRB DLAs and super-DLAs above or within 1 σ of the threshold would be larger if their $N_{\rm HI}$ values are larger by a factor of ∼ 2.) (2) In this sense, the quasar super-DLAs are more similar to the GRB absorbers than are the quasar DLAs. Indeed, given that the GRB DLAs are believed to arise in star-forming regions within the main body of the galaxies (e.g., Pontzen et al., 2010), quasar super-DLAs are also likely to arise in quasar sightlines with small impact parameters to the absorber galaxies. (3) The H_2 covering fraction is significant for several super-DLAs above the "obscuration threshold", suggesting that they have higher molecular content than the DLA population. This is consistent with the observations of H_2 in 5 out of 7 quasar super-DLAs by Noterdaeme, Petitjean, and Srianand (2015b). Overall, it appears that the quasar super-DLAs are likely to arise more often in molecule-rich environments than the quasar DLAs. (See section 3.3.5 below for discussion of a search for molecular gas in the super-DLAs studied here.)

3.3.4 SEARCH FOR LYMAN-α EMISSION

As discussed in Section 1.3.1, previous studies of super-DLAs have shown strong emission lines. The super-DLA towards Q1135-0010, in particular, shows strong emission lines of of Lyman-α, H-α, and [O III], which implies a SFR $\sim$ 25 $M_\odot$ yr^{-1} (Kulkarni et al., 2012; Noterdaeme et al., 2012b), which is much higher than typical DLAs. This could indicate a larger galaxy.

Of our two super-DLAs, only the system towards Q0230-0334 showed a hint of weak Lyman-α emission near the center of the super-DLA trough. After resampling the ESI spectrum to a wavelength dispersion of 1.5 Å, we measured an integrated Lyman-α emission flux of $(3.41 \pm 1.03) \times 10^{-17}$ erg s^{-1} cm^{-2}, while the SDSS spectrum gives a integrated flux of $(3.66 \pm 1.50) \times 10^{-17}$ erg s^{-1} cm^{-2}. These fluxes correspond to a SFR of 1.55 ± 0.47 $M\odot$ yr^{-1} based on the ESI data (or 1.66 ± 0.66 $M\odot$ yr^{-1} based on the SDSS spectra) assuming $L_{Ly-\alpha}/L_{H-\alpha} = 8.7$ for case-B recombination and adopting the Kunnicutt (1998) relation between the SFR and H-α luminosity. However, if dust extinction is present, then the SFR will be higher.

3.3.5 SEARCH FOR MOLECULES

For Q0230-0334 and Q0743+1421, the ESI spectra did not cover either the Lyman or Werner band absorption lines of H_2 for the super-DLA observers. However, for both absorbers, several lines of CO were covered, but none were detected. For the non-detections of the line near 1477 Å in the absorber rest frame, the strongest line covered, we have 3 σ upper limits on column densities given in table 3.10. In order to obtain N_{H_2} and more definitive N_{CO} values higher S/N and lower wavelength spectra for Q0230-0334 and Q0743+1421 are required. If our super-DLAs indeed have low molecular contents despite having log $N_{HI} \geq 21.7$, that would contrast with observations of the Galactic ISM, which shows a sharp increase in H_2 column densities at log $N_{HI} \geq 20.7$ (e.g., Savage et al., 1977); however, low molecular contents would be consistent with the low SFRs in our super-DLAs suggested by the marginal or weak detections of Lyman-α emission in the DLA troughs.

	Q0230-0334	Q0743+1421
log N_{COJ0}	< 13.41	< 13.56
log N_{COJ1}	< 13.71	< 13.86
log N_{COJ2}	< 13.71	< 13.86
log N_{COJ3}	...	< 14.12
log N_{COJ4}	...	< 14.12
log N_{COJ5}	...	< 14.12
log N_{COJ6}	...	< 14.12
Total log $N_{COJ0-J6}$	...	< 14.85

Table 3.10 N_{CO} 3 σ Upper Limits For Super-DLAs

3.3.6 GAS KINEMATICS

Previous studies of DLAs have noted a correlation between metallicity and gas velocity dispersion (e.g., Ledoux et al., 2006; Meiring et al., 2007; Som et al., 2015), which could, if the gas velocity dispersion is measure of the mass of the absorber, indicate a mass-metallicity relationship in the absorbing galaxies, or velocity dispersion could reflect turbulent motions or outflows.

Our velocity dispersion Δv_{90} measurements for the two super-DLAs, Q0230-0334 and Q0743+1421 are shown in figure 3.9. These measurements were made on well-detected, unsaturated lines: Fe II λ2250 and Cr II λ2056 for Q0230-0334 and Q0743+1421, respectively giving values of Δv_{90} = 149.9 km s^{-1} and 67.9 km s^{-1}.

(While higher wavelength resolution spectra would give more reliable determinations of Δv_{90}, our values are reasonable approximations given that they are quite distinct from each other and feasible at the spectral resolution of our data.) While, $\Delta v_{90} = 67.9$ km s^{-1} found for Q0743+1421 is surprising low, Noterdaeme et al. (2015a) found a $\Delta v_{90} = 28$ km s^{-1} in a N$_{HI}$ = 22.4 super-DLA at $z_{abs} = 2.34$ towards Q2140-0321.

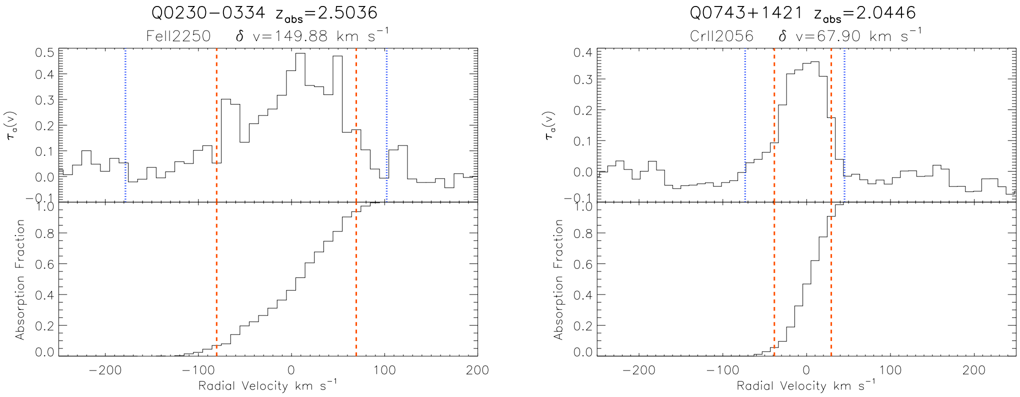

Figure 3.9 Estimates of velocity dispersions for a representative line in each of the two super-DLAs observed in this study. The top and bottom sub-panels for each absorption line shows the apparent optical depth profile and the absorption fraction as functions of the velocity of the absorbing gas relative to the stated redshift. The red dashed vertical lines mark the 5% and 95% levels of absorption. The blue dotted vertical lines in each of the top sub-panels show the full range of velocities used to make the measurements.

Figure 3.10 plots the velocity dispersion vs. the H I column density in order to compare the kinematics of regular DLAs and super-DLAs. The vertical and horizontal dashed lines denote log N$_{HI}$ = 21.7 and $\Delta v_{90} = 160$ km s^{-1}. It is interesting to note that 20% of the DLAs (those with log N$_{HI}$ < 21.7) have $\Delta v_{90} > 160$ km s^{-1}, while 10% of the super-DLAs have such large velocity dispersions.

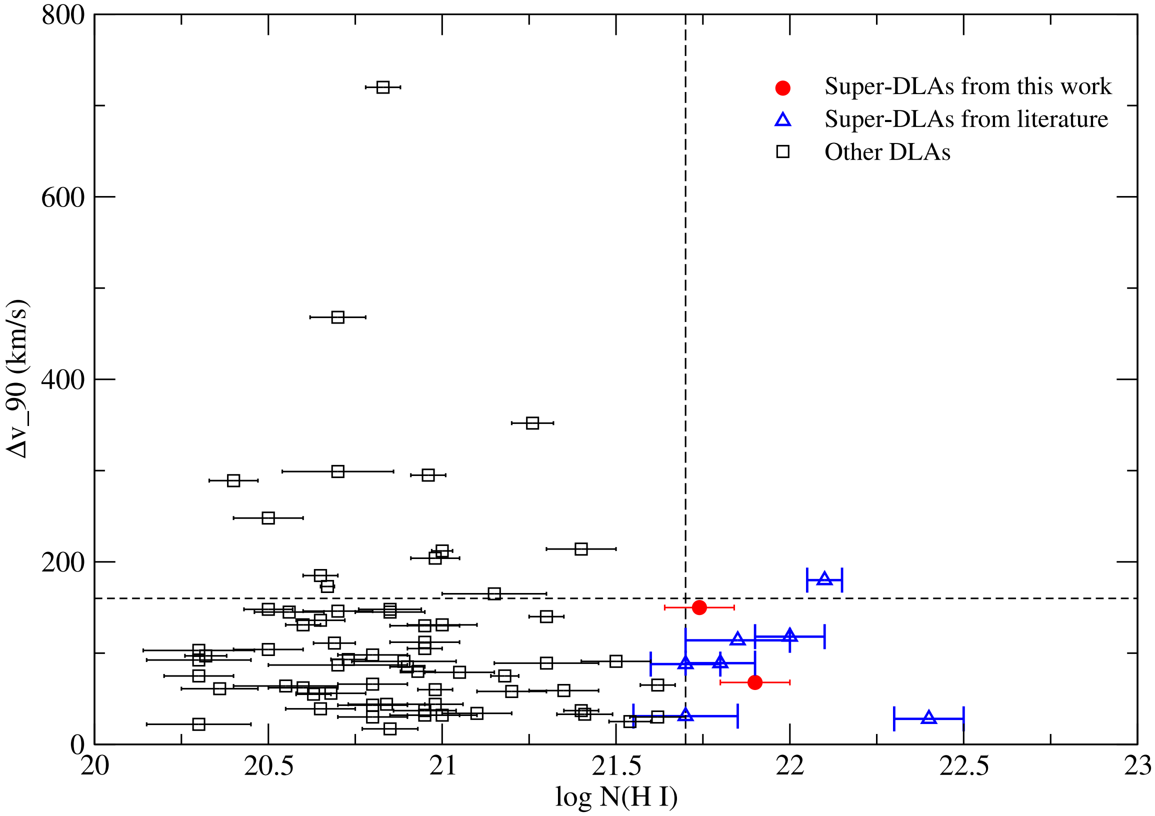

Figure 3.10 Plot of velocity dispersion vs. H I column density for DLAs and super-DLAs. Super-DLAs appear to have a somewhat smaller incidence of large velocity dispersions than other DLAs.

CHAPTER 4

CONCLUSION AND FUTURE WORK

4.1 CONCLUSION

4.1.1 CONCLUSION: MOLECULAR ABSORPTION IN DLAS

For the sub-mm sample, photometric measurements were obtained for 10 quasars that had absorbers with redshifts $0.652 < z_{abs} < 3.104$ taken with the SPIRE on Herschel. Of these 10 objects, 3 showed fluxes > 1 Jy. In addition, we have analyzed spectra for 5 other DLAs ($0.524 < z_{abs} < 1.173$) that were taken with SPIRE and HIFI on Herschel. Of these spectra, two targets, the DLA towards PKS0420-014 at $z = 0.633$ and the DLA towards AO0235+164 at $z = 0.52385$, showed very tentative detections of $C^{18}O$, and another, the DLA towards TXS0827+243 at $z = 0.52476$, showed a very tentative detection of HCO. We report 3 σ upper limits for several other molecules.

4.1.2 CONCLUSION: METAL & MOLECULAR ABSORPTION IN SUPER-DLAS

We have analyzed spectra of two especially gas-rich DLAs ("super-DLA"s) from Keck ESI and measured abundances of a number of elements. Both absorbers show remarkably similar metallicities of ~ -1.3 to ~ -1.4 dex and comparable, definitive depletion levels, as judged from [Fe/Zn] and [Ni/Zn]. One of the absorbers show supersolar [S/Zn] and [Si/Zn]. Using potential detections of weak Ly-α emission at the bottom of the DLA trough for Q0230-0334, we estimate SFR in the absorbers to be $\sim$1.6 $M_\odot$ yr^{-1}. Finally, measurements of the velocity spread Δv_{90} suggest that super-DLAs may have narrower velocity dispersions and may arise in cooler and/or less turbulent gas.

Our study has further demonstrated the potential of super-DLAs as unique laboratories to study the physical and chemical properties of potentially star-forming interstellar gas in distant galaxies. Observations of a larger super-DLA sample at higher S/N are essential to further understand the nature of these unique absorbers and how their underlying galaxies compare with those probed by the moderate DLAs, and also those probed by the GRB DLAs.

4.2 Future Work

Although significant steps to understanding molecular and atomic absorption in DLAs and super-DLAs have been made, there are still many unanswered questions.

4.2.1 Future Work: Molecular Absorption in Distant Galaxies

Although we have increased the sample of molecular absorption, much still remains to be answered. Higher S/N data for a larger sample is required to gain a complete picture. The larger sample will allow for a better understanding of molecular abundances and physical conditions such as temperature and density of the absorber gas. This in turn will allow a comparison between the distant ISM and the Milky Way ISM allowing for an understanding of how the ISM evolves with time. Molecular abundances will also constrain the temperature of the cosmic microwave background at the absorption redshift, which will allow a constraint on the $\mathrm{T_{CMB}}$ vs redshift relation and determine how it compares with the expected relationship based on the standard cosmological model, $\mathrm{T_{CMB}} = 1.725(1+z)$.

Atacama Large Millimeter/Submillimeter Array (ALMA)

Although Herschel Space Observatory is a powerful instrument, its limited lifetime and aperture has limited its use. We plan to use the Atacama Large Millimeter/Submillimeter Array (ALMA) to conduct follow up observation on our Herschel observations and to expand the sample of molecular absorption systems. ALMA is an interferometer located in the desert in Chile, and will have excellent resolution. In addition, being a ground based array, it will not have the limited lifetime due to cooling that limited Herschel. These properties will allow for more and longer observations staggered out overtime to maximize the observed flux.

4.2.2 Future Work: Super-DLA Atomic and Molecular Absorption

Although we have significantly increased the sample of Super-DLAs, many questions still remain, including the nature of these absorbers and how their underlying galaxies compare with moderate DLA host galaxies. There is also still the question as to how Quasar super-DLAs compare with DLAs probed by GRBs. Questions also remain as to the nature of molecular clouds in super-DLAs and how the molecular fraction correlates with their metallicity, dust depletion and SFR density. In order to answer these questions observations of a larger super-DLA sample at higher S/N is essential.

A larger sample is also necessary to understand the SFR density and gas kinematics of super-DLAs. An estimate of the cooling rate and thus SFR density is needed to examine whether SFR density and gas surface density correlate in super-DLAs, as is seen in nearby galaxies. The current sample shows a smaller velocity dispersion than regular DLAs, as shown in Fig. 3.10, which suggests they have cooler or less turbulent gas. In addition, high S/N spectra is required to search for rare elements such as Cu, Co, and s-process elements Ga, Ge, which will allow supernova nucleosynthesis and star formation histories to be constrained.

Bibliography

Asplund, M. et al. (2009). *ARAA* 47.481.

Battistini, C. and T. Bensby (2015). *A&A* 577.A9.

Berg, T. A. M et al. (2015). *PASP* 127.167.

Boissé, P. et al. (1998). *A&A* 333.841.

Bravo, E. and G. Martinex-Pinedo (2012). *PhRvC* 85.055805.

Cucchiara, A. et al. (2015). *ApJ* 804.51.

Ellison, S. L. et al. (2012). *MNRAS* 424.293.

Guimaraes, R. et al. (2012). *AJ* 143.147.

Heinmuller, J. et al. (2006). *A&A* 449.33.

Jenkins, E. B. (2009). *ApJ* 700.1299.

Jenkins, E. B. et al. (2005). *ApJ* 623.767.

Khare, P. et al. (2007). *A&A* 464.487.

Kramida, A. et al. *NIST Atomic Spectra Database (ver. 5.1)*. URL: `http://physics.nist.gov/asd` (visited on 2013).

Krumholz, M. R., C. F. McKee, and J. Tumlinson (2009b). *ApJ* 699.850.

Krumholz, M. R. et al. (2009a). *ApJ* 701.L12.

Kulkarni, V. P. et al. (2007). *ApJ* 661.88.

Kulkarni, V. P. et al. (2010). *NewA* 15.735.

Kulkarni, V. P et al. (2012). *ApJ* 749.176.

Kulkarni, V. P et al. (2015). *ApJ* in press (arXiv: astro-ph/1510.05342).

Kunnicutt, R. C. (1998). *ApJ* 498.541.

Ledoux, C. et al. (2006). *A&A* 457.71.

Ledoux, C. et al. (2009). *A&A* 506.661.

Lehner, N. et al. (2013). *ApJ* 770.138.

Meiring, J. D. et al. (2006). *MNRAS* 370.43.

Meiring, J. D. et al. (2007). *MNRAS* 376.557.

Menten, K. M. et al. (2008). *A&A* 492.725.

Momjian, E. et al. (2014). *AJ* 147.6.

Morton, D. C. (2003). *ApJS* 149.205.

Müller, H. S. P. et al. (2005). *JMoSt* 742.215.

Neufeld, D. A. et al. (2010). *A&A* 518.L108.

Noterdaeme, P., P. Petitjean, and R. Srianand (2015b). *A&A* 578.L5.

Noterdaeme, P. et al. (2007). *A&A* 474.393.

Noterdaeme, P. et al. (2008). *A&A* 481.327.

Noterdaeme, P. et al. (2012a). *A&A* 547.L1.

Noterdaeme, P. et al. (2012b). *A&A* 540.63.

Noterdaeme, P. et al. (2014). *A&A* 566.24.

Noterdaeme, P. et al. (2015a). *A&A* 577.A24.

Omont, Alain (2007). *Reports on Progress in Physics* 70.1099.

Péroux, C. et al. (2003). *MNRAS* 346.1103.

Péroux, C. et al. (2006). *MNRAS* 386.2209.

Pettini, M. (2004). “Element Abundances through the Cosmic Ages”. *XIII Canary Islands Winter School of Astrophysics, Cosmochemistry: The Melting Pot of Elements, Eds. C. Esteban, R. J. Garcí López, A. Herrero & F. Sánchez.*

Pickett, H. M. et al. (1998). *Journal of Quantitative Spectroscopy and Radiative Transfer* 60.883.

Pontzen, A. et al. (2010). *MNRAS* 402.1523.

Prochaska, J. X. et al. (2001). *ApJS* 137.21.

Prochaska, J. X. et al. (2003). *ApJS* 147.227.

Prochaska, J. X. et al. (2007). *ApJ* 666.267.

Rafelski, M. et al. (2012). *ApJ* 755.89.

Rafelski, M. et al. (2014). *ApJ* 782.L29.

Rouch, M. (1998). *ARAA* 36.267.

Savage, B. D. and K. R. Sembach (1991). *ApJ* 379.245.

Savage, B. D. and K. R Sembach (1996). *ARAA* 34.279.

Savage, B. D. et al. (1977). *ApJ* 216.291.

Savaglio, S. et al. (2012). *MNRAS* 420.627.

Schaye, J. (2001). *ApJ* 562.L95.

Scheinis, A. I. et al. (2002). *PASP* 114.851.

Shu, F. (1991). *The Physics of Astrophysics.* Mill Valley, Ca, USA: University Science Books.

Som, D. et al. (2015). *ApJ* 806.25.

Spitzer, L. (1978). *Physical Processes in the Interstellar Medium.* Mill Valley, Ca, USA: Wiley & Sons.

Steidel, C. C. (1990). *ApJ* 74.37.

Storrie-Lombardi, L. J. and A. M. Wolfe (2000). *ApJ* 543.552.

van den Hoek, L. B. and M. A. T. Groenewegen (1997). *A&AS* 123.305.

Vreeswijk, P. M. et al. (2004). *A&A* 419.927.

Wiklind, T. and F. Combes (1996). *Nature* 379.139.

— (1998). *ApJ* 500.129.

Woosley, S. E. and T. A. Weaver (1995). *ApJS* 101.181.

York, D.G. et al. (2000). *AJ* 120.1579.

Zheng, W. et al. (1997). *ApJ* 495.469.

APPENDIX A

REDSHIFT

Redshift, or Doppler shift, is the principle that light waves can be stretched towards the red end of the spectrum. Traditionally, this is due to relative motion of the light source and observer. However, cosmologically the redshift is a parameter that represents the expansion of the universe. It is defined as

$$z = \frac{\lambda_{obs} - \lambda_{rest}}{\lambda_{rest}}. \tag{A.1}$$

The cosmological redshift be related to the Doppler redshift by thinking of it resulting from the recession velocity of the source. This Doppler redshift is give by

$$\lambda_{obs} = \lambda_{rest}\sqrt{\frac{1+\beta}{1-\beta}}, \tag{A.2}$$

where, $\beta = (v/c)$ and v is the apparent recessional speed with respect to the observer. Therefore, for very small recessional speeds, $v \ll c$, Eq. A.1 can be rewritten as

$$z = \frac{\lambda_{obs} - \lambda_{rest}}{\lambda_{rest}} = \frac{v}{c}. \tag{A.3}$$

APPENDIX B

SOLAR SYSTEM ABUNDANCES

Table B.1 Solar system abundances (from Asplund et al., 2009), in logarithmic units, for various elements commonly seen in the ISM.

Element	Solar Abundance Relative to H
He	-1.07
C	-3.57
N	-4.17
O	-3.31
Na	-5.76
Mg	-4.40
Al	-5.55
Si	-4.49
P	-6.59
S	-4.88
Cl	-6.50
Ar	-5.60
Ca	-5.66
Ti	-7.05
Cr	-6.36
Mn	-6.57
Fe	-4.50
Co	-7.01
Ni	-5.78
Cu	-7.81
Zn	-7.44

Appendix C

Line Measurements

C.1 Radiative Transport and Optical Depth

The amount of energy in a given wavelength range $d\lambda$ that passes through a surface element dA which subtends a solid angle $d\Omega$ from a point source of radiation in time dt is given by

$$dE_\lambda = I_\lambda \cos\theta dA\, d\Omega\, d\lambda\, dt, \tag{C.1}$$

where θ is the angle between a ray of light and the normal to the surface, and I_λ is defined as the specific intensity.

If, in addition to the point source, the intervening medium adds photons, then the amount of energy added in a volume element dV is given by

$$dE_\lambda = j_\lambda\, dV\, d\lambda\, dt\, d\Omega = j_\lambda\, dA\, ds\, d\Omega\, d\lambda\, dt, \tag{C.2}$$

where j_λ is the emissivity of the medium and ds is the path along the beam within dV. The contribution of dV to the beam intensity is given by

$$dI_\lambda = j_\lambda ds. \tag{C.3}$$

If, in the intervening medium absorbs photon in addition to emitting, then the resulting reduction in beam intensity is

$$dI_\lambda = n(s)\sigma_\lambda I_\lambda ds \equiv \alpha_\lambda I_\lambda ds, \tag{C.4}$$

where n is the number density of absorbing particles, σ is the absorption cross section, and α_λ is called the attenuation coefficient. The differential equation describing the change in beam intensity along the path length ds, known as the transfer equation, becomes

$$\frac{dI_\lambda}{ds} = j_\lambda - \alpha_\lambda I_\lambda \tag{C.5}$$

when taking into account the emission an absorption of intervening material. This can be arranged as

$$\frac{dI_\lambda}{ds\ \alpha_\lambda} = \frac{j_\lambda}{\alpha_\lambda} - I_\lambda. \tag{C.6}$$

By defining the 'optical depth' as

$$\tau_\lambda = \int \alpha_\lambda ds = \int n(s)\sigma_\lambda ds, \tag{C.7}$$

and the 'source function' of the medium as

$$S_\lambda \equiv \frac{j_\lambda}{\alpha_\lambda}, \tag{C.8}$$

Equation C.6 can be re-written as

$$\frac{dI_\lambda}{d\tau_\lambda} = S_\lambda - I_\lambda. \tag{C.9}$$

If the source function is assumed to be constant along the beam, equation C.9 can be integrated to get

$$I_\lambda(\tau_\lambda) = I_\lambda(0)e^{-\tau_\lambda} + S_\lambda(1 - e^{-\tau_\lambda}), \tag{C.10}$$

where $I_\lambda(0)$ is the incident intensity of the beam on the medium. If the medium has no emission and is responsible for only absorption, then the source term goes to zero and equation C.10 reduces to

$$I_\lambda(\tau_\lambda) = I_\lambda(0)e^{-\tau_\lambda}. \tag{C.11}$$

This is the functional form of intensity with respect to the wavelength of a beam of light passing through an absorbing medium.

This equation is essentially the function of an absorption spectrum when applied to the scenario of absorption from intervening material along a line-of site towards a bright background source. The quantity $I_\lambda(0)$ represents the unaffected spectrum of the background source and I_λ represents absorption signatures imprinted on the background spectrum by intervening gas which can be characterized by τ_λ. The optical depth, which, as shown by equation C.7, includes information on important properties of the absorbing gas, is one of the fundamental observables derived from the study of absorption lines present in the spectra of background sources. True densities, $n(s)$, along a line-of-sight are extremely difficult, if not impossible, to determine from most astrophysical observations and especially absorption spectra. However, the 'column density' given by

$$N \equiv \int n(s)ds \tag{C.12}$$

gives quantitative information on absorbing particles. The column density is defined as the number of absorbing particles (e.g., neutral atoms, ions or molecules) along the line of sight in a 1cm^2 cross-section beam. Using this, equation C.7 can be written as

$$\tau_\lambda = N\sigma_\lambda. \tag{C.13}$$

Using equation C.13 and measurements of the absorption lines produced by different molecules or elements in various ionization stages, column densities can be determined. These column densities can be used to gain an understanding of the chemical composition, ionization, and other physical properties of the absorbing gas.

C.2 Equivalent Width

Equivalent width is an observable easily derived from an absorption line with no real assumptions. It is a fundamental observable that can be used to derive other values of importance. The equivalent width, W, is defined as

$$W \equiv \int_0^\infty \frac{I_c - I_\lambda}{I_c} d\lambda = \int_0^\infty (1 - e^{-\tau_\lambda}) d\lambda \tag{C.14}$$

where I_λ is the intensity within the absorption line and I_c is the continuum intensity. The continuum intensity is defined as the intensity of the region in background spectrum adjacent to the absorption line but unaffected by any absorption. When dealing with continuum normalized spectrum $I_c = 1$, and the equivalent width can be defined as the width of a rectangular box with unit height and with the same area as enclosed by the spectral line, as shown in Figure C.1

When measuring the equivalent width of an absorption line of a cloud at redshift z_{abs} the observed frame equivalent width (W_{obs}) is stretched by a factor of $(1 + z_{abs})$ when compared to rest frame equivalent width (W_{rest}). Therefore,

$$W_{rest} = \frac{W_{obs}}{(1 + z_{abs})} \tag{C.15}$$

can be used to find the rest frame equivalent width.

C.3 THE CURVE OF GROWTH

The relationship between the equivalent width, W_λ, and the column density of absorbing atoms is called the curve of growth (COG). Therefore, it can be used to derive the column density from the observed W_λ. For any given absorption line the optical depth at the core of the line, τ_0, determines the function dependence of W_λ on N. There are three distinct regions to the COG that depend on the values of τ_0 and N, a Linear region, a Logarithmic region, and a Damped region as shown for Lyman-α in Figure C.2.

C.3.1 LINEAR PART OF THE COG

The linear part of the COG is seen for optically thin lines, $\tau_0 \ll 1$. In this regime we can use the approximation $e^{-x} \simeq 1 - x$, which using equations C.13, C.14 and D.18 gives us

$$W_\lambda = N\sigma_0 \int_{-\infty}^{\infty} \phi_\lambda d\lambda = N\sigma_0, \tag{C.16}$$

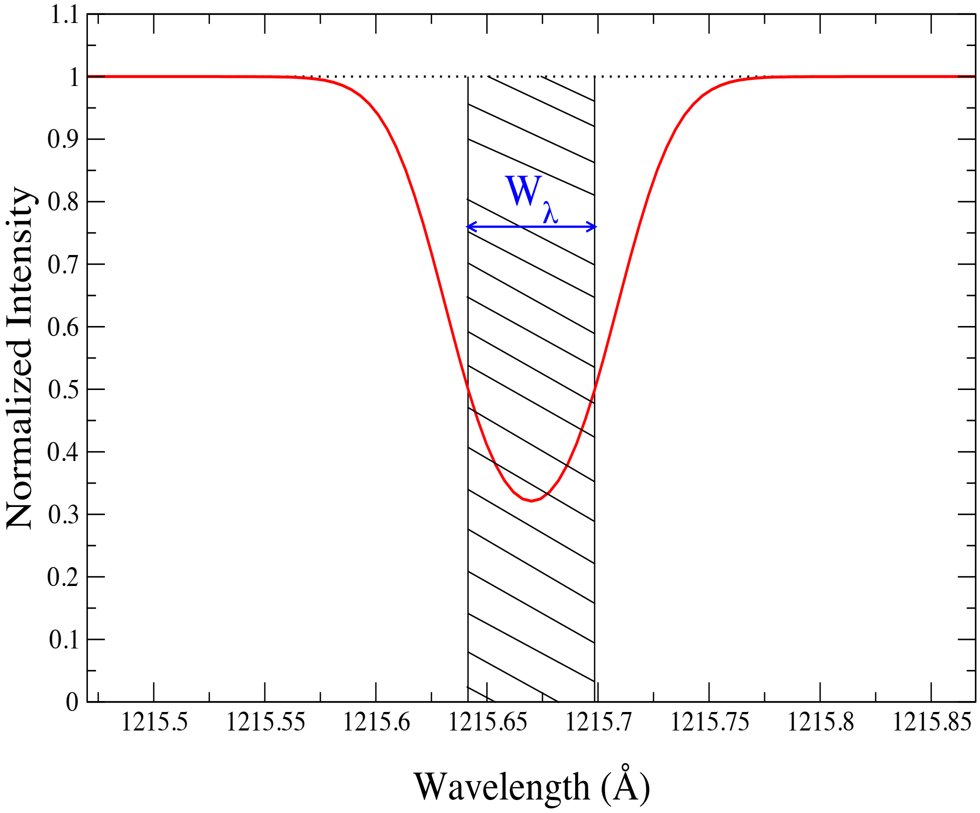

Figure C.1 The equivalent width of an absorption line (the width of the rectangle), where the area under the line profile is same with the area of the rectangular shaded region of unit height. The horizontal dashed line represents the normalized continuum ($I_c = 1$), and the absorption line is represented with the solid red curve.

with ϕ_λ representing a probability distribution ($\int_{-\infty}^{\infty} \phi_\lambda = 1$). Using a numerical value of σ_0, we get

$$N = 1.13 \times 10^{20} \frac{W_\lambda}{\lambda^2 f} \mathrm{cm}^{-2}. \tag{C.17}$$

This relationship exhibits that, in this region, $N \propto W_\lambda$ and independent of b. Therefore in the linear part of the COG, W_λ provides an accurate determination of N.

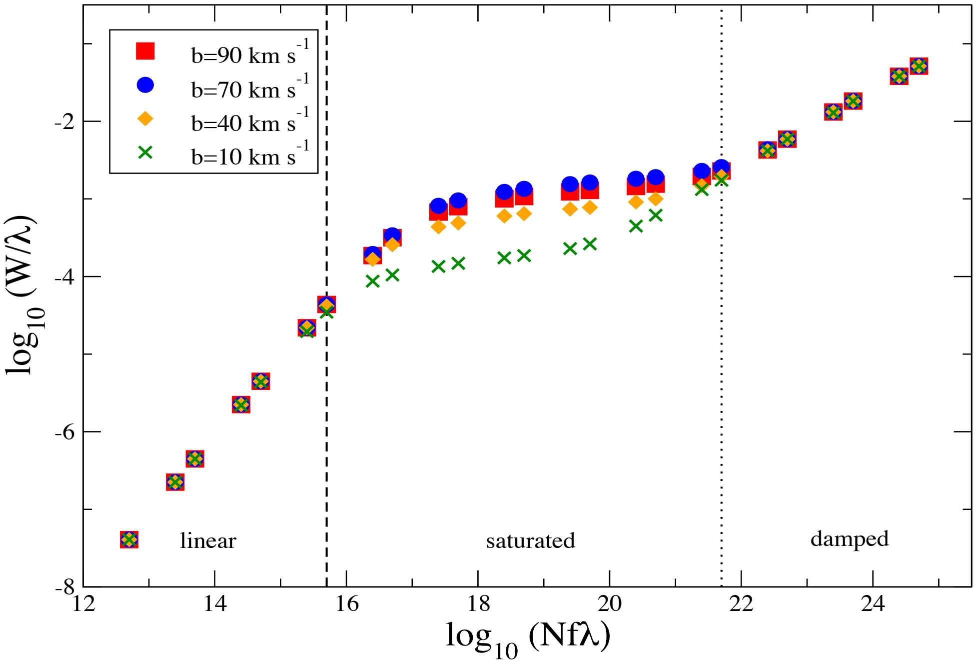

Figure C.2 The Curve of Growth function of the equivalent width with respect to the column density for the Lyman-α line of Hydrogen corresponding to b-parameters of 10, 40, 70, and 90 km s^{-1}. The equivalent width is independent of the b-parameter in the linear (log $N_{HI} \leq 17.2$) and the damped (log $N_{HI} \geq 19$) regions.

C.3.2 Logarithmic Part of the COG

Once a line has zero residual intensity at the core of the absorption line (all of the photons at the core of the line are absorbed), an increase in τ_0 (i.e. an increase in N), produces very little increase in W_λ with increasing N (few additional photons are removed from the beam), which by definition means the line is 'saturated'. This part of COG is seen for $10 \lesssim \tau_0 \lesssim 10^3$. Here $W_\lambda \propto b\sqrt{\ln(N/b)}$, and therefore the growth function becomes sensitive to the Doppler b-parameter. Due to this, in the logarithmic part of the COG, W_λ is not an accurate measure of N.

C.3.3 Damped Part of the COG

The damped part of the COG is seen with an increase in τ_0 beyond the logarithmic region. In this part of the COG, an increase in column density causes the optical depth to increase to significant levels at wavelengths far from the core of the line, where absorption is dominated by natural damping. This leads to damping wings (where $\sigma_\lambda \propto \Delta\lambda^{-2}$) and an increase of the equivalent width as $W_\lambda = 2(N\sigma_0\gamma)^{1/2}$ Å. Therefore, in this region ($\tau_0 \gtrsim 10^4$) the equivalent width is independent of the b-parameter, allowing for an accurate determination of the column density. Figure C.2 suggests that the damped region, $\tau_0 \gtrsim 10^4$, corresponds to $N_{HI} \gtrsim 10^{19}$ for Lyman-α.

C.4 Abundances of Elements

The abundance of an element X with respect to Y, given the column densities N_X and N_Y respectively, can be calculated by

$$[X/Y] = \log(N_X/N_Y) - \log(N_X/N_Y)_\odot \tag{C.18}$$

where $\log(N_X - N_Y)_\odot$ is the solar abundance ratio between elements X and Y. When calculating the abundance with respect to H using

$$[X/H] = \log(N_X/N_H) - \log(N_X/N_H)_\odot \tag{C.19}$$

it is called the absolute abundance of the element X. The solar abundances are determined from measurements of the Sun's photosphere or from the composition of meteorites. The solar abundance pattern used for this work comes from Asplund et al. (2009) and is given in Table B.1.

APPENDIX D

ABSORPTION LINE STRUCTURE

The structure of the absorption lines is governed by the physical and chemical properties of the absorbing gas. This structure is a signature of the modification of the background source radiation by the intervening material's optical depth. Although the absorption profiles of atomic transitions or single molecular transition are expected to be extremely sharp and well defined, they are observed to be much more complex and broad. The shape and width of a spectral line is determined by several factors such as the column density of the absorbing ion, and the temperature, turbulence and bulk motion in the gas.

D.1 SUB-STRUCTURES

Sub-structures exist within the absorption lines. These sub-structures are the result of individual gas clouds moving with different relative velocities with respect to each other within the galaxy. Therefore, a spectral line is composed of multiple lines produced by the different velocity components blended to result in a complex absorption feature.

D.2 LINE BROADENING

How photons of light interact with intervening media depends on their own energies as well as the energy structure of the atoms in the medium. A photon of energy $h\nu_0 = E_u - E_l$ can be absorbed, making an atom transition to an excited state, when interacting with an atom with energy levels E_u and E_l (where $E_u > E_l$). The excited atom will remain in that unstable state for a short time (typically $\sim 10^{-8}s$ for dipole transitions) before spontaneously emitting a photon of the same energy ($h\nu_0$) and returning to the lower energy state. However, unlike the incident photon traveling along the beam direction, the spontaneous emission can be emitted in any random direction in an isotropic probability distribution, which essentially removes a photon with frequency ν_0 from the sight line. A large collection of such atoms, like that of a gas cloud, will have a cumulative effect that will result in an absorption line in the spectrum of the background source at $\nu = \nu_0$, that theoretically will have a delta-function profile. However, in addition to sub-structures causing individual delta-function profiles, there exist additional mechanism responsible for the complex nature of absorption lines. The two main processes at work in the typical ISM are natural broadening and Doppler broadening.

D.2.1 Natural Broadening

The first broadening process that gives observed lines finite widths is quantum mechanical broadening. Quantum mechanical broadening is due to the fact that atoms takes a finite amount of time for de-excitation, which by obeying the uncertainty relation $\Delta E \Delta t \sim \hbar$, gives an energy difference between two states that spreads the energy, E, around the value given by $E_{ul} = E_u - E_l$. This spread in energy ΔE translates into the finite width of the absorption line. Using the damped oscillator model for atomic transitions (ie. the classical treatment), the absorption cross section, σ_ν, can be found to be

$$\sigma_\nu = \left(\frac{\pi e^2}{m_e c}\right) \phi(\nu) = \left(\frac{\pi e^2}{m_e c}\right) \frac{\gamma/4\pi^2}{(\nu - \nu_0)^2 + (\gamma/4\pi)^2}, \tag{D.1}$$

where γ is the oscillator damping constant, and the σ_ν is a spectral line profile centered at ν_0. Equation D.1 takes the form of a Lorentzian profile with full width at half maximum of FWHM$= \gamma/2\pi$. When the full quantum mechanical treatment is utilized, the absorption cross section yields the same cross section with a multiplication factor called the oscillator strength f, which describes the probability of the transition in question, which is given by

$$g_l f_{ul} = g_u A_{ul} \frac{m_e c \lambda^2}{8\pi^2 e^2}, \tag{D.2}$$

where λ is in Å, g_u and g_l are the statistical weights of the upper and lower energy levels, respectively and A_{ul} is the transition probability. This fully quantum form of the absorption cross section, including the oscillator strength is given as

$$\sigma_\nu = \left(\frac{\pi e^2}{m_e c}\right) f_{ul} \phi(\nu). \tag{D.3}$$

Different bound-bound transitions arise from different oscillator strength, typically with $f \lesssim 1$, with only a few very strong transitions having $f > 1$. Oscillator strengths corresponding to various transitions can be determined analytically (for H), numerically, or from laboratory measurements, and can be thought of as the effective number of classical oscillators (Shu, 1991). The absorption cross section can be written in terms of the wavelength λ as

$$\sigma_\lambda = \sigma_0 \phi_\lambda, \tag{D.4}$$

where σ_0 in the equation above is given by

$$\sigma_0 = \frac{\lambda^4}{8\pi c} \frac{g_u}{g_l} A_{ul}, \tag{D.5}$$

where the broadening function, ϕ_λ, is given as

$$\phi_\lambda = \frac{1}{\pi} \frac{\gamma}{\gamma^2 + (\lambda - \lambda_0^2)}, \tag{D.6}$$

and the radiation damping constant is given by

$$\gamma = \frac{\lambda^2}{4\pi c} \sum_{E_r < E_u} A_{ul}. \tag{D.7}$$

The naturally broadened profile has a FWHM, in wavelength units, of FWHM = $\lambda^2 \gamma / 2\pi c$, which for most UV and Optical transitions bands is very small.

D.2.2 Doppler Broadening

While the natural broadening of a line around the central wavelength ν_0 can be explained by natural broadening through the absorption cross section described in equation D.3, the Doppler motion of individual atoms can shift the central wavelength. Additionally, absorption lines can be broadened by differences in the relative velocities of atoms in the gas. These differences in velocity arise primarily from bulk motion and thermal motion, with the thermal motion arising from collisions in the gas that thermalize the medium and produce a Maxwellian velocity distribution in a short amount of time (Spitzer, 1978). According to the relativistic Doppler effect, the difference between observed and rest-frame wavelengths is dependent on the velocity as

$$\lambda_{obs} = \lambda_{rest}\sqrt{\frac{1+\frac{v}{c}}{1-\frac{v}{c}}}. \tag{D.8}$$

In non-relativistic conditions where $v/c << 1$, which exists at the temperatures typical for interstellar gas, equation D.8 reduces to

$$\lambda_{obs} = \lambda_{rest}(1 \pm \frac{v_x}{c}), \tag{D.9}$$

where the radial component of the velocity is taken to be in the x direction. According to the Maxwellian velocity distribution, the number of particles with velocities between v and $v + dv$ is

$$N(v)dv = \frac{N_0}{\sqrt{\pi}b}\exp(-v_x^2/b^2)dv, \tag{D.10}$$

where N_0 is the total number of particles in the cloud and the ‘Doppler b-parameter’, b, is the most probable speed, defined as

$$b = b_{th} = \sqrt{\frac{2kT}{m}}. \tag{D.11}$$

The Maxwell-Boltzmann distribution of velocities, in combination with equation D.9, gives the fraction of atoms absorbing radiation between the wavelengths λ and $\lambda + d\lambda$

as

$$\psi(\lambda)d\lambda \equiv \frac{N(\lambda)d\lambda}{N_0} = \frac{1}{\sqrt{\pi}\Delta\lambda_D}\exp\left(-\frac{\lambda - \lambda_{rest}^2}{\Delta\lambda_D^2}\right) \tag{D.12}$$

where the the Doppler width, $\Delta\lambda_D$ is defined as

$$\Delta\lambda_D = \frac{\lambda_{rest}b_{th}}{c}. \tag{D.13}$$

The Maxwell-Boltzmann distribution of velocities, given by equation D.12, represents a Gaussian profile with full width at half max of FWHM $= 2\sqrt{\ln 2}\Delta\lambda_D$. Through numerical evaluation of equation D.13, a FWHM dependent on the temperature in Kelvin, T, and the atomic mass number A is found to be FWHM $\sim 0.22\sqrt{T/A}$ km s^{-1}. In addition to thermal motions, entire clouds can move with respect to the observer's reference frame as bulk motions, while smaller turbulent motions within the clouds contributes to spectral line broadening. In order to account for this effect, a term can be added to the Doppler parameter, defining an 'effective Doppler parameter'

$$b_{eff}^2 = b_{th}^2 + b_{turb}^2. \tag{D.14}$$

In ideal spectra, it is possible to separate the turbulent and thermal motions from observed spectra to determine the kinetic temperature of the gas. This is possible due to the mass dependence of the Doppler parameter, causing different atomic species within a given absorber to have different thermal broadening of their absorption features while the effect of turbulence will be the same. If an absorbing cloud contains lines of species (e.g., Si and Fe) with very different masses, it is possible to estimate the temperature by measuring the FWHM of the lines independently and by eliminating b_{turb}, allowing the temperature to obtained from

$$T = \frac{m_{Si}m_{Fe}(b_{Si}^2 - b_{Fe}^2)}{(m_{Fe} - m_{Si})2k}. \tag{D.15}$$

Realistically, according to Jenkins et al. (2005), high resolution and high S/N spectra are needed for accurate parameter estimates, but even high resolution spectra can exhibit blending of individual lines that can lead to artificially high Doppler parameters and hence temperatures.

D.3 VOIGT PROFILES

While Natural and Doppler broadening are independent processes, they have a combined broadening effect on a spectral line. This combined effect is know as a Voigt profile and is the convolution of the Natural and Doppler broadening functions:

$$\phi_\lambda(Voigt) = \phi_\lambda(Natural) \otimes \psi_\lambda(Doppler). \tag{D.16}$$

Using equations D.6 and D.12 we get,

$$\phi_\lambda(Voigt) = \frac{1}{\pi^{3/2}\,\Delta\lambda_D} \int_{-\infty}^{\infty} \frac{\gamma}{\gamma^2 + (\lambda - \lambda')^2} \exp\left[-\frac{(\lambda - \lambda')^2}{\Delta\lambda_D^2}\right] d\lambda'. \tag{D.17}$$

This can be used to write the absorption cross section:

$$\sigma_\lambda = \sigma_0 \phi_\lambda(Voigt). \tag{D.18}$$

Which, using equations C.11 and C.13, can be used to write the column density of the absorbing species as

$$I_\lambda = I_0 e^{-N\sigma_0\phi_\lambda(Voigt)}. \tag{D.19}$$

By equating D.6 and D.12, it can seen be that at $\Delta\lambda \times (\frac{c}{\lambda}) \simeq 3b$, for the values of A_{lu} of commonly seen interstellar absorption lines, the probabilities of absorption due to these broadening processes are comparable. With $\Delta\lambda < \frac{3b\lambda}{c}$ the Voigt profile of the absorption is dominated by the Dopper broadening, while with $\Delta\lambda > \frac{3b\lambda}{c}$, the absorption is dominated by natural broadening. Figure D.1 shows the Voigt profiles of absorption lines for several different N (with a fixed b-parameter) and b-parameter (with a fixed N) values to depict how N and b affect the profile.

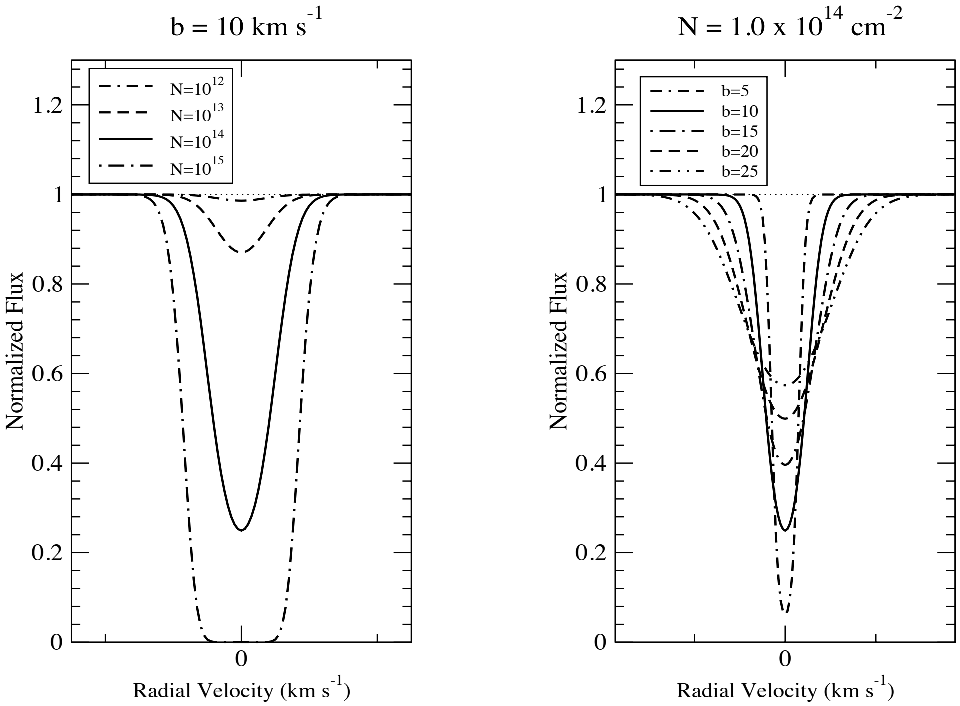

Figure D.1 Left panel: Theoretical Voigt profiles for the Fe II 1608 Å transition with $b = 10$ km s^{-1} and column densities of $10^{12} cm^{-2}$, $10^{13} cm^{-2}$, $10^{14} cm^{-2}$, and $10^{15} cm^{-2}$. Right panel: Theoretical Voigt profiles for the Lyman-α line of Hydrogen with $N = 1.0 \times 10^{14} cm^{-2}$ and b-parameters of 5, 10, 15, 20, and 25 km s^{-1}. The horizontal dotted line in both panels represents the normalized continuum level.

D.4 INSTRUMENT SPREAD FUNCTION (ISF)

An additional effect on the profile is the instrument spread function (ISF). The ISF is the contribution from imperfections in the optics, diffraction gratings, and detectors. This effect results in an observed spectral profile that is a convolution of the ISF and the theoretical Voigt profile:

$$I_{obs}(\lambda) = \left[I_0(\lambda) e^{-\tau_\lambda} \right] \otimes \phi_{ISF}(\lambda), \tag{D.20}$$

or from equation D.18,

$$I_{obs}(\lambda) = \left[I_0(\lambda)e^{-N\sigma_0\phi_\lambda(Voigt)}\right] \otimes \phi_{ISF}(\lambda). \tag{D.21}$$

The ISF can be derived from observations of emission lines of gas discharge lamps in the laboratory which have small natural widths that can be calculated from Eq. D.3. Therefore, the observed line profiles can be used to determine the ISF. Typically, the ISF can be approximated as a Gaussian. With this knowledge, the column densities of the ion in interest can be extracted from their absorption line profiles by Voigt profile fitting via χ^2 minimization.

APPENDIX E

THE APPARENT OPTICAL DEPTH

One way to derive the column densities is the ‘Apparent Optical Depth’ (AOD) method. This method, described in Savage and Sembach (1991), uses the Apparent Optical Depth of the observed line profile. The apparent optical depth is the instrumentally blurred optical depth. This method assumes that the spectral continuum of the background source usually varies slowly with wavelength. Therefore we can assume a nearly constant continuum level over the extent of the absorption line, provided a small line width, allowing equation D.20 to be rewritten as

$$I_{obs}(\lambda) = I_0(\lambda)[e^{-\tau_\lambda} \otimes \phi_{ISF}(\lambda)] \tag{E.1}$$

Using equation E.1, the apparent optical depth is found to be

$$\tau_a(\lambda) = \ln[I_0(\lambda)/I_{obs}(\lambda)] = \ln[1/(e^{-\tau_\lambda} \otimes \phi_{ISF}(\lambda))] \tag{E.2}$$

When lines are well resolved, FWHM(ϕ_{ISF}) « FWHM(line), the apparent optical, $\tau_a(\lambda)$, is a good approximation for the true optical depth, τ_λ. Using this knowledge, the AOD can be written in terms of the column density:

$$\tau_a(\lambda) = \frac{\pi e^2}{m_e c^2} f \lambda^2 N(\lambda) \tag{E.3}$$

where $N(\lambda)d\lambda$ is the column density between λ and $\lambda + d\lambda$ and $N = \int N(\lambda)d\lambda$ is the total column density. When this relationship is written in terms of radial velocity, it becomes

$$\tau_a(v) = 2.654 \times 10^{-15} f \lambda N(v) \tag{E.4}$$

when the wavelength λ is given in terms if Å. Using the equation E.2 and E.4, the total column density can be written as

$$N = \int N(v)dv = \frac{3.768 \times 10^{14}}{f\lambda} \int \ln\left(\frac{I_0(v)}{I(v)}\right) dv \qquad \text{(E.5)}$$